Chapter 2
Oceanographical and Geological Background

Pinxian Wang and Qianyu Li

Introduction

The South China Sea (SCS) embraces an area of about 3.5×10^6 km^2 and extends from the Tropic of Cancer to the Equator, across over 20 degrees of latitude in the west Pacific. Since the last decade, the SCS has become the focus in studying the East Asian monsoon, like the Arabian Sea for the Indian monsoon (Wang B. et al. 2003). The SCS offers an ideal locality for high-resolution paleoceanographic researches in the low-latitude western Pacific because its hemipelagic sediments often register higher deposition rates and its carbonate compensation depth (CCD) is generally deeper than neighboring sea basins (Wang P. 1999).

Geographically, the SCS is located in between Asia and the Pacific, the largest continent and the largest ocean on earth. To its north and west, the SCS is bordered by South China and Indochina Peninsula; to the east and south, it is surrounded by a chain of islands, ranging from Luzon in the north to Borneo in the south. The continent side to the northwest and west is basically a mountainous land with a narrow coastal plain except for deltas of large rivers such as the Pearl River, the Red River and the Mekong River. Mountains reach 1,000–1,300 m high in South China and generally 1,600–2,000 m in Indochina. A mountain range, Truong Son Ra or Annam Cordillera, extends along the Vietnam coast with a northern peak of 3,142 m. Islands on the southeastern side are also mountainous, peaking at 4,101 m in Borneo and 3,997 m in Taiwan (Liu Y. 1994). The contrast in geodynamics between the NW continental side and the SE island side has given rise to a number of distinguished features in SCS oceanography and sedimentology. This chapter provides an overview of the major oceanographic and geological features of the SCS.

P. Wang (✉)
State Key Laboratory of Marine Geology, Tongji University, Shanghai 200092, China
e-mail: pxwang@online.sh.cn; pxwang@tongji.edu.cn

Q. Li
State Key Laboratory of Marine Geology, Tongji University, Shanghai 200092, China;
School of Earth and Environmental Sciences, The University of Adelaide,
South Australia 5005, Australia
e-mail: qli01@tongji.edu.cn; qianyu.li@adelaide.edu.au

P. Wang, Q. Li (eds.), *The South China Sea*, Developments in Paleoenvironmental Research 13, DOI 10.1007/978-1-4020-9745-4_2,

2.1 Bathymetry and Geomorphology

The bathymetry of the SCS comprises three parts: the deep basin, the continental slope and the continental shelf, respectively covering about 15%, 38% and 47% of the total area with an average water depth of about 1,140 m. The major feature of the SCS topography is the rhomboid deep basin, which overlies oceanic crust and extends from NE to SW (Fig. 2.1). Water depth in the deep basin averages ∼4, 700 m, with a maximum depth of 5,559 m reported from its eastern margin yet to be confirmed by survey. The deep basin is divided by a chain of sea mounts along 15 °N, or "Central Ridge", into two sectors: a relatively shallower northeastern part, and a deeper southwestern part (Wang Y. 1996).

The central deep basin is surrounded by continental and island slopes, topographically dissected and often studded with coral reefs (Fig. 2.2). The northern slope with Dongsha reef island and the western slope with Xisha (Paracel Islands) and Zhongsha reefs (Macclesfield Bank) are separated by the Xisha Trough, while the southern slope is occupied by the Nansha Islands (Spratly Islands), the largest reef area in the SCS. The Nansha Islands are scattered on a carbonate platform known as "Dangerous Grounds", covering a broad area of ∼570, 000 km^2. The eastern slope is narrow and steep, bordered by the deep-water Luzon Trough and Manila Trench (Figs. 2.1 and 2.2).

The continental shelf is well developed on the northern and southern sides of the SCS (Figs. 2.1 and 2.2). Both the northern and southern shelves are narrower to the east and broader to the west. On the northern shelf, there are a number of submarine deltas developed off the Pearl and other river mouths, and fringing reefs are growing along the coasts of Leizhou Peninsula and Hainan Island. Exceeding ∼300 km in width, the Sunda Shelf in the southwestern SCS is one of the largest shelves in the world. A number of submerged river valleys observed on the bottom of the Sunda Shelf are relict of a large river network, the Paleo-Sunda Rivers, during the last glacial maximum (LGM).

Although the SCS is open at present on its northeastern and southwestern sides, it has been highly sensitive to sea level changes in the past glacial cycles as a semi-enclosed basin. The southern connection to the Indian Ocean is limited to the uppermost 30–40 m and completely closed at glacial sea level lowstands, as was also the connection to the East China Sea/Okinawa Trough through Taiwan Strait in the northeast. Deeper passages exist only along its eastern side: the Bashi (Luzon) Strait with water depth of ∼2, 400 m connecting to the open Pacific or, to be precise, the western Philippine Sea, and both the Mindoro Strait of ∼420 m and the Balabac Strait of ∼100 m connecting to the Sulu Sea (Fig. 2.3; Table 2.1). During the LGM, therefore, the SCS was largely closed except the two passages along the east boundary which remained open to the Pacific and to the Sulu Sea respectively.

The rhomboid shape of the SCS basin, together with its NE-SW topographic axis and broader northern and southwestern shelves (Fig. 2.3), may exert a significant impact on atmospheric and oceanographic circulation. The coastal ranges block the monsoon wind flows toward the land and give rise to a wind jet, which drives the

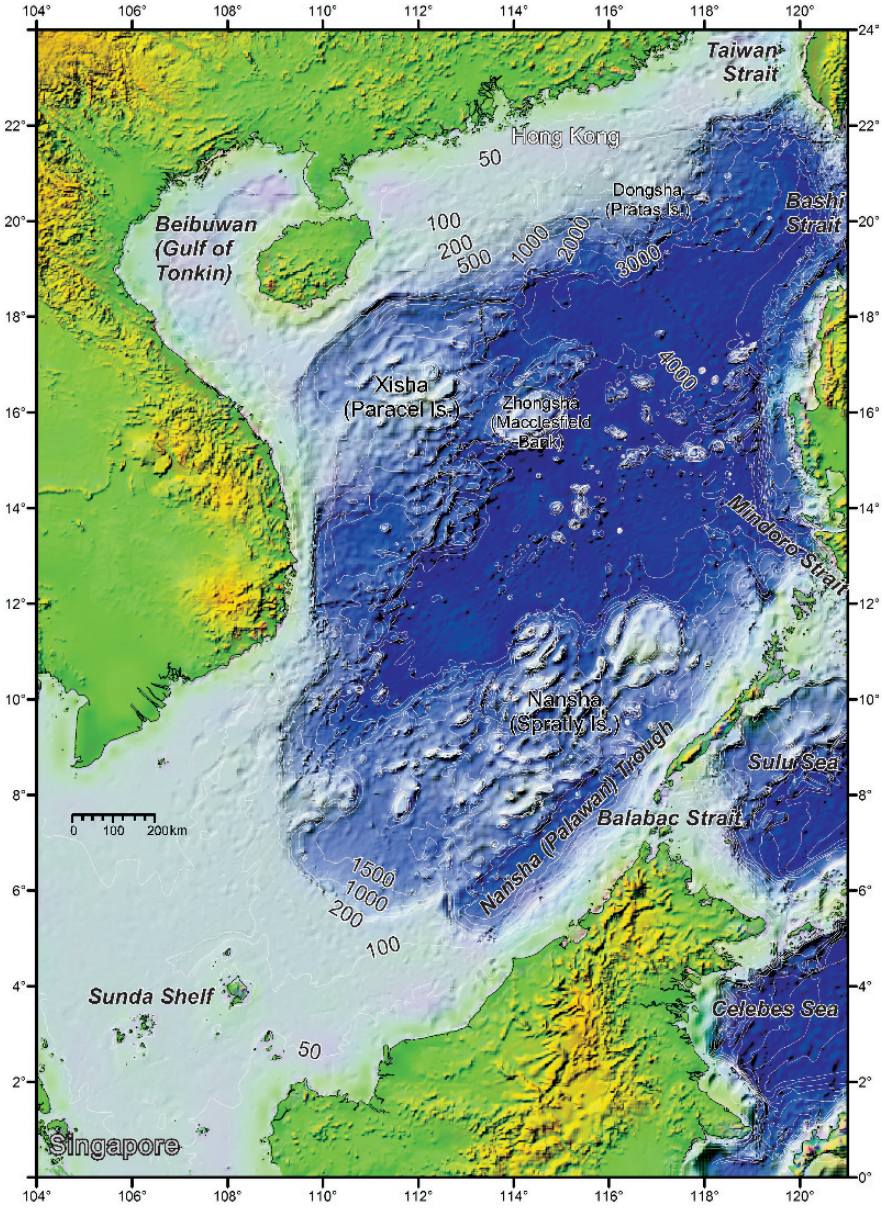

Fig. 2.1 Map shows the major topographic features of the South China Sea (SCS) and neighboring sea basins. Isobaths are in meters (m)

surface currents of the sea roughly along the basin axis with seasonal reversal in direction (Xie et al. 2003; Liu Q. et al. 2004). As shown below, this jet divides the SCS into two halves with different oceanographic features.

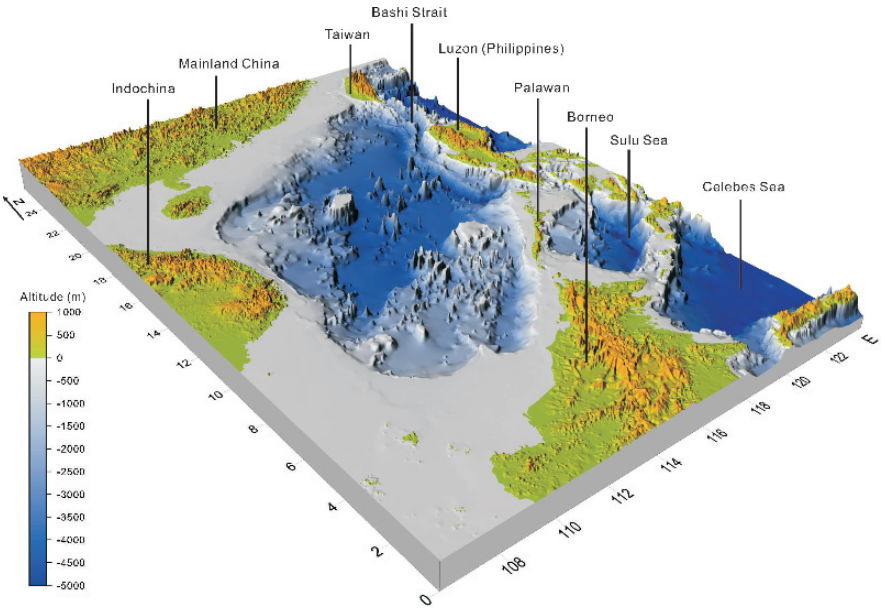

Fig. 2.2 Three-dimensional diagram shows the main geomorphologic features of the SCS (modified from Wang P. 1999)

Table 2.1 Straits of the SCS are mostly shallow except the Bashi Strait (compiled from various sources)

Strait	Connecting to	Sill depth	Minimal width	Fig. 2.3
Taiwan	East China Sea	70 m	130 km	P1
Bashi (Luzon)	Philippine Sea	2,400 m	370 km	P2
Mindoro	Sulu Sea	420 m	125 km	P3
Balabac	Sulu Sea	100 m	~50 km	P4
Karimata	Java Sea	~50 m	150 km	P5
Malacca	Andaman Sea	25 m	37 km	P6

2.2 Oceanography

The oceanography of the upper water of the SCS is largely dictated by two factors: the underlying morphology of the enclosed basin, and the overlying atmospheric circulation especially the East Asian Monsoon. The deep-water oceanography of the SCS is much less studied, but appears to be controlled by its only deep connection to the open ocean, the Bashi Strait. Despite of significant recent progress in the modern SCS oceanography, many paleoceanographic publications are still citing old literature. Here we provide an update of the current knowledge on the SCS oceanography, which is highly relevant to the interpretation of paleo-records, especially those concerning the Asian monsoon, upper water structure, exchanges with the Pacific and other sea basins, surface and deep circulations, productivity and biogeochemistry.

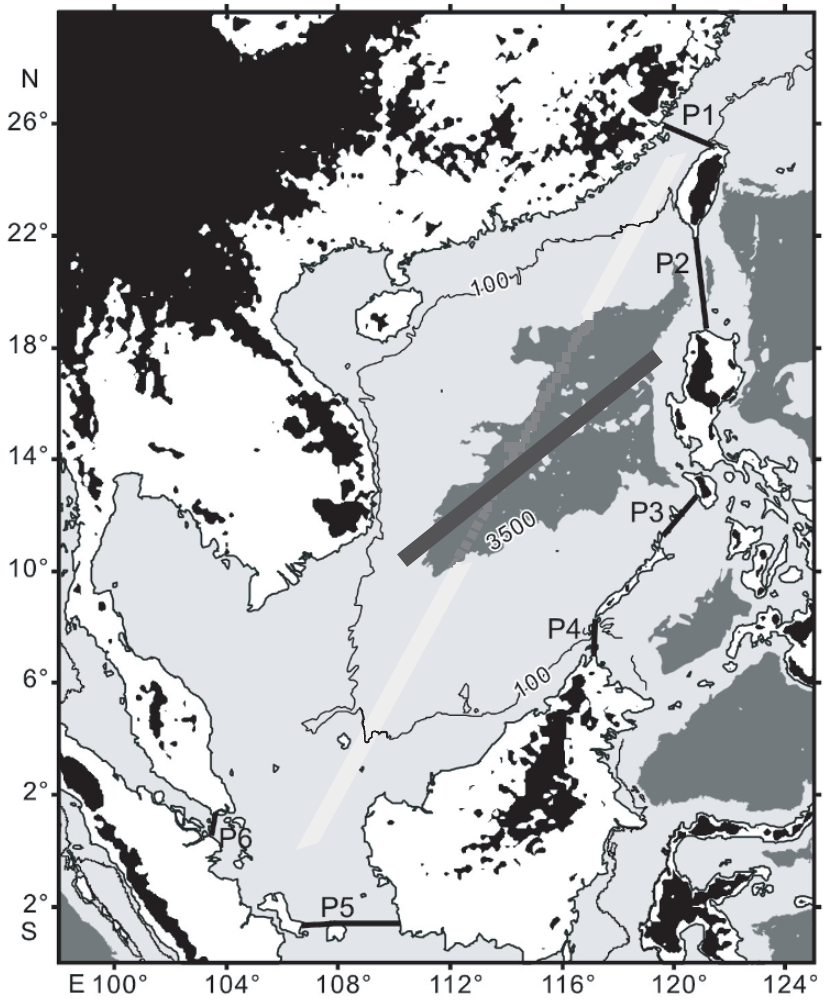

Fig. 2.3 Major topographic features of the SCS basin and environs are shown with black areas indicating +500 m elevation, white areas 500–0 m, light grey areas 0–3,500 m water depth, and dark grey areas deeper than 3,500 m. The NE-SW bar marks the oceanographic divide between the northern and southern parts of the SCS. Short black bars are passages: P1 = Taiwan Strait, P2 = Bashi (Luzon) Strait, P3 = Mindoro Strait, P4 = Balabac Strait, P5 = Karimata Strait, P6 = Malacca Strait

Monsoon

Monsoon is the prevailing climate feature in Asia, including the SCS. The Asian monsoon is the largest monsoon system in the modern world, and its two subsystems, the Indian or South Asian Monsoon and the East Asian Monsoon, are closely

related and interact with each other, but they have different structures shaped by diverse sea-land configuration patterns. For East Asia, the ocean is to the east and the Tibetan Plateau to the west; while South Asia has the ocean to the south and the Tibetan Plateau to the north. At least three major distinctions have resulted from these sea-land configuration patterns. (1) For the South Asian subsystem, the winter monsoon is largely blocked by Tibet and hence is much weaker than its summer counterpart, whereas East Asia has the most intensive winter monsoon system in the world. (2) The South Asian summer monsoon is tropical in nature, while the East Asian monsoon has a subtropical in addition to the tropical component (Chen L. 1992). (3) East Asia humidity originates in the western Pacific warm pool (WPWP).

In winter, there are three branches of monsoon flows over the Arabian Sea, the Bay of Bengal (Indian monsoons) and the SCS (East Asian monsoon), forming strong cross-equatorial northerlies there (Fig. 2.4B). Only the northerly over the SCS can be traced backward to its origin over the cold Siberia, from where the world's coldest winter air-mass runs southward along the East Asian coastal zone, generating the strongest winter monsoon, which is in a sharp contrast to that in South Asia.

The East Asian summer monsoon comprises a tropical component connected with cross-equatorial flows from the south and an additional eastern component originated from the subtropical easterlies in the western periphery of the West Pacific subtropical high. Along with the western North Pacific monsoon trough or the ITCZ (the inter-tropical convergence zone) there is an East Asian subtropical front or "Meiyu (plum rain) front", resulting in two major summer monsoon areas in East Asia (Fig. 2.4) (Wang B. et al. 2003). The winter and summer monsoons affect the SCS with different strength and in different time duration. The winter monsoon lasts nearly six months (November to April), while the weaker summer season lasts only nearly 4 months (mid-May to mid-September) (Chu and Wang 2003). The mean surface wind stress over the SCS averages nearly $0.2\,N/m^2$, reaching $0.3\,N/m^2$ in the central portion in December but dropping to nearly $0.1\,N/m^2$ in June. These features underline the necessity to distinguish winter vs summer monsoon in paleo-records which, unsurprisingly, often display a more complicated relationship with the orbital forcing than the Indian and African monsoons. In addition, care is necessary in correlating land-sea monsoon records. For example, the "South China Sea Monsoon Experiment (SCSMEX)" (1996–2001) found that a strong (weak) monsoon over the SCS usually leads to lesser (more) precipitation over the middle and lower reaches of the Yangtze River basin, and more (lesser) precipitation in North China (Ding et al. 2004).

As mentioned above, the East Asian monsoon differs from the Indian monsoon by its intensive winter monsoon flows and an additional subtropical component due to the unique land-ocean configuration (Fig. 2.4). Moreover, the interannual variability of the Asian monsoon associated with El Niño-Southern Oscillations (ENSO) is also much more significant in the East Asian sector than in the Indian sector. Therefore, large changes in the Pacific thermal conditions may greatly alter the intensity of the East Asian monsoon but not the Indian monsoon (Wang B. et al. 2003).

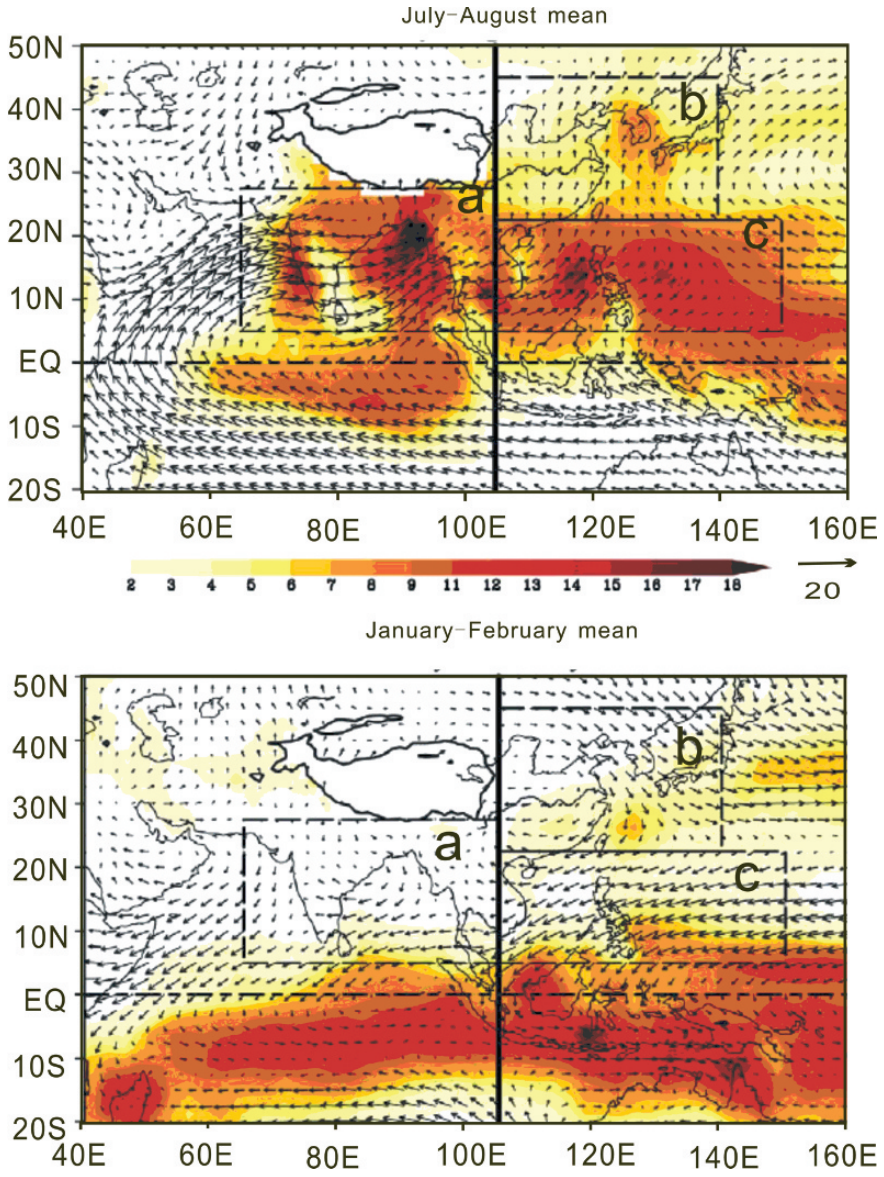

Fig. 2.4 Asian monsoon system is shown in climatological mean precipitation rates (*shaded* in mm/day) and 925 hPa wind vectors (*arrows*) during July–August (*upper panel*) and January–February (*lower panel*). The three major summer precipitation areas include (**a**) Indian tropical monsoon, (**b**) East Asian subtropical monsoon and (**c**) western North Pacific tropical monsoon (modified from Wang B. et al. 2003)

The low-level wind patterns over the SCS are affected by orographic features of the surrounding land. In winter, the northeasterly monsoon prevails the SCS, and two wind speed maxima exceeding 10 m s^{-1} occur respectively in the Taiwan and

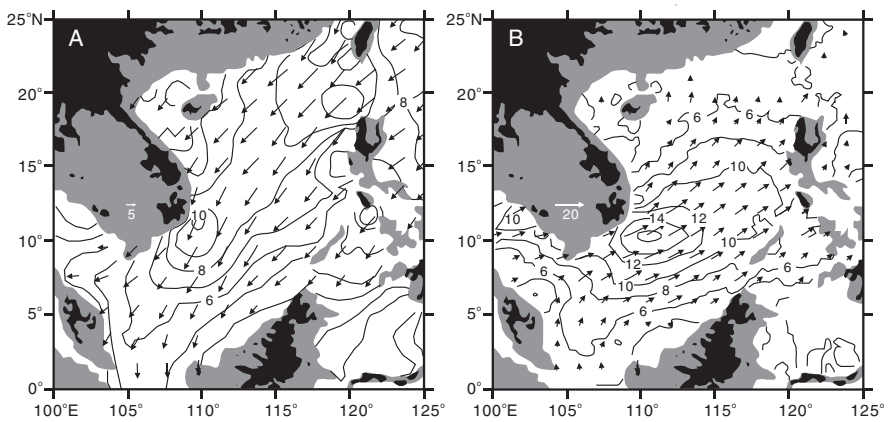

Fig. 2.5 QuikSCAT surface winds over the SCS are shown by (**A**) winter wind velocity (vector) and its magnitude (contours at 2 m/s intervals) averaged for December–February 2000–2002, and (**B**) summer wind stress vectors and their magnitude (contours in $10^{-2}\mathrm{Nm}^{-2}$) averaged for June-August 2000–2002. Land topography with elevations >500 m is *shaded* in *black* and 0–500 m in *grey*. Note that the wind jet with maximal velocity is in NE-SW direction (modified from Xie et al. 2003 and Liu Q. et al. 2004)

Bashi straits and around 11 °N off the coast of southern Vietnam near the southern tip of Annam Cordillera (Fig. 2.5A). Both wind maxima result from orographic forcing by mountains. The northeasterly winds are blocked by the Indochina coastal mountain range, giving rise to a wind jet offshore, similar to the southwesterly jet in summer (Fig. 2.5B) (Xie et al. 2003; Liu Q. et al. 2004).

Surface Circulation

Much understanding has been gained about the surface circulation in the SCS since the pioneering work of Wyrtki (1961). Using both hydrographic and ship-drift data, Wyrtki provided the first picture of the surface circulation pattern in the SCS, basically a cyclonic gyre in winter and an anticyclonic gyre in summer, and suggested them to be results of the seasonally reversing monsoon winds. Later, the Wyrtki model of circulation patterns was confirmed by dynamical studies (e.g., Shaw and Chao 1994; Liu Z. et al. 2001) and observations (review by Su 2004). These distinct features are in fact reflections of the upper-layer circulation in response to the seasonal changes of the monsoon wind-stress curl, with additional influence from the Kuroshio in its northern part (Qu 2000). In winter, there is a basin-wide cyclonic gyre (Fig. 2.6A), while in summer the circulation splits into a weakened cyclonic gyre north of ∼12 °N and a strong anti-cyclonic gyre in the south (Fig. 2.6B).

The large-scale features of the seasonal surface circulation of the SCS can be demonstrated with the distribution of climatological mean January and July dynamic heights (dyn cm) at 100 m water depth (Fig. 2.7), which shows a large cyclonic gyre in winter (Fig. 2.7B), dominant north of the line roughly from 10 °N, 110 °E to

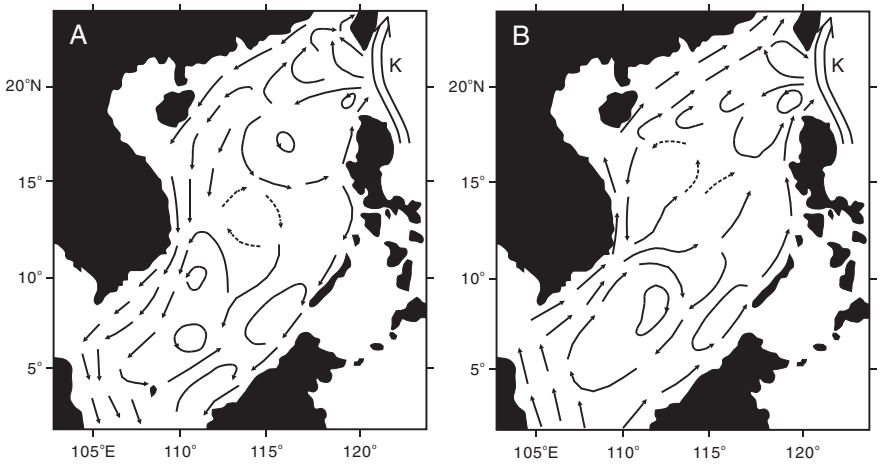

Fig. 2.6 Surface circulation of the modern SCS shows opposite patterns between (A) winter and (B) summer (modified from Fang et al. 1998). The Kuroshio Current is labeled with "K"

15 °N, 120 °E, and two gyres in summer (Fig. 2.7C). A large cyclonic eddy, the West Luzon Eddy, is present west of Luzon in winter and another strong cyclonic eddy, the East Vietnam Eddy, occurring off central Vietnam in both winter and summer (Qu 2000; Su 2004). Because the winter gyre is much stronger, the above-mentioned line separates the SCS into the northern and southern parts with different oceanographic features as discussed below.

Both satellite imageries and dynamic computations reveal a cross-basin wind-induced summer surface jet flowing northeastward from the central Vietnam to Luzon. The maximum speed of the current reaches 0.25 m/s near Vietnam bight at the surface, and declines to 0.20 m/s at 50 m water depth. If the orientation of the maximum velocity is defined as the axis, it extends from 110 °E, 10 °N to 120 °E, 18 °N at 50 m depth (Chu and Wang 2003), which is about the same as the boundary between the southern and northern parts of the SCS (Fig. 2.3; Qu 2000; Su 2004) and close to the axis of maximum monsoonal winds described above (Xie et al. 2003; Liu Q. et al. 2004).

The SCS surface circulation, therefore, can be summarized into a schematic diagram with seasonally alternating basin-scale gyres (Fig. 2.8). Associated with these gyres are strong western boundary currents. In winter, a southward jet flows along the entire western boundary. In summer, a northward jet flows along the western boundary in the southern SCS, apparently veering eastward off central Vietnam near 12 °N″ (Wang G. et al. 2006). This cross-basin eastward jet, or "Summer Southeast Vietnam Offshore Current" of Fang et al. (2002), has a maximum velocity of around 0.8 m/s and plays a significant role in the SCS oceanography by dividing it into the northern and southern parts. The eastward jet is accompanied by a dipole structure with an anticyclonic cell south of the jet and a cyclonic cell north of it. On average the dipole structure begins in June, peaks in strength in August or September, and disappears in October (Wang G. et al. 2006; Liu K. et al. 2002).

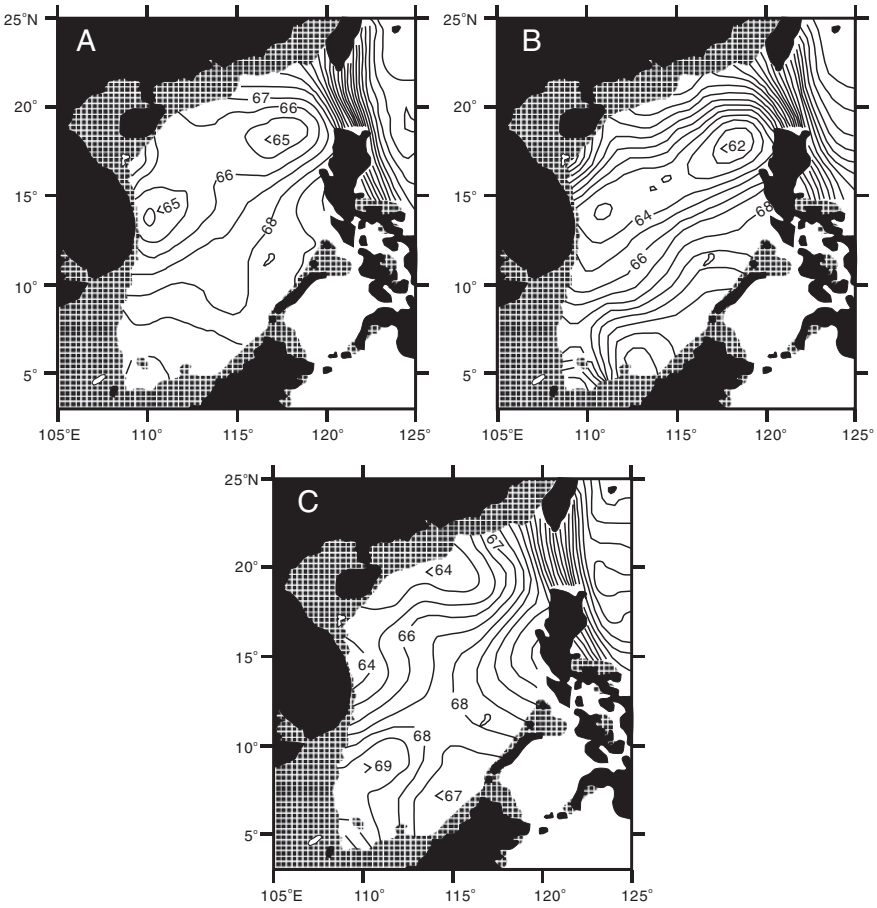

Fig. 2.7 Distribution of the mean dynamic heights (contour in dyn cm) at −100 m in the SCS is shown for three periods: (**A**) annual mean, (**B**) January monthly mean and (**C**) July monthly mean (modified from Qu 2000). Region with water depth shallower than 100 m is stippled

Surface Temperature and Salinity

The seasonal reversal in circulation leads to seasonal contrasts in sea surface temperature (SST) and salinity (SSS) patterns. In summer, surface water temperature in the SCS is uniform, with only insignificant variations between 28.5 and 29.5 °C (Fig. 2.9B). In winter, an intense western boundary current flows southward on the continental slope, separating the Sunda Shelf to the west and the deep basin to the east (dashed line in Fig. 2.8). This current transports cold water from the north and causes a distinct cold tongue south of Vietnam, leading to a steeper temperature gradient in the winter SCS (Fig. 2.9A). Compared to the neighboring Pacific and Indian Oceans, the winter SST in the SCS are considerably lower and form a conspicuous gap in the Indo-Pacific Warm Pool (Liu Q. et al. 2004).

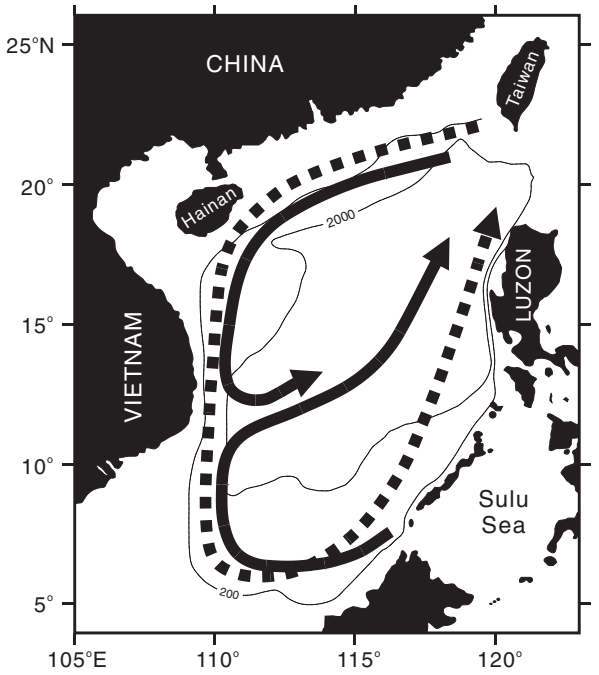

Fig. 2.8 A sketch map illustrates the main surface circulation of the SCS featuring seasonally alternating, basin-scale cyclonic gyres: winter (*dashed line*); summer (*solid line*). The summer pattern involves a cyclonic gyre in the northern and an anticyclonic gyre in the southern parts (based on Wang G. et al. 2006 and Liu K. et al. 2002)

Precipitation exceeds evaporation in the SCS, especially in the southern part. The surface salinity varies between 32.8 and 34.2‰ and thus preconditions the SCS for an "estuarine-basin" circulation. In winter, salinity is higher in the north due to the Kuroshio influence, with a high-salinity tongue in the top 100 m north of 12 °N propagating to the southwest. The winter salinity decreases southward because of increasing precipitation, resulting in isohalines running parallel to latitudes (Fig. 2.9C). In summer, salinity varies less in the northern SCS but very large in the southern part, with higher values off the Vietnam coast due to summer upwelling and a low-salinity tongue outside the Mekong estuary (Fig. 2.9D). Freshwater input is a significant factor for the surface salinity distribution. For example, the Pearl River plume has a distinct monsoonal behavior and influences strongly the hydrographic characteristics nearby the river mouth. Waters near the Pearl River mouth is highly stratified especially during the wet season, with a strong halocline inside the estuary and a plume formed in the surface layer just outside the estuary (Fig. 2.10). Soon after forming, the plume turns toward the west during the dry season, but turns to the east in the wet season due to the southwesterly monsoon (Dong et al. 2004). Once the surface plume reaches beyond the inner shelf, it can easily extend further east across the shelf, possibly driven by the SCS Warm Current and the favorable southwesterly summer monsoon winds (Fig. 2.10E). The bottom current, however, continues to the west outside the estuary along the coast like a density current because of the diminishing effect of the winds below the stratified layer (Su 2004). Therefore, a proper understanding of the plume behavior outside

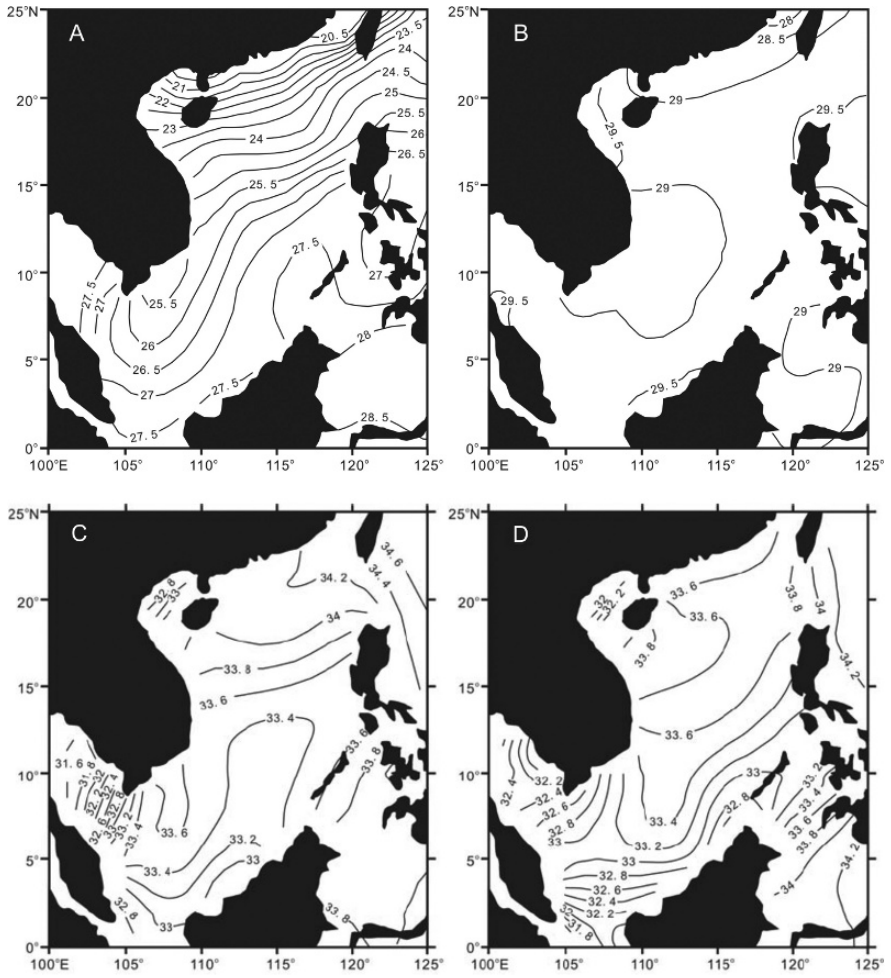

Fig. 2.9 Sea surface temperature (°C) and salinity (‰) in the modern SCS show distinct seasonality patterns: (**A**) SST in winter; (**B**) SST in summer; (**C**) SSS in winter; (**D**) SSS in summer (Wang D. et al. 2002)

the estuary is crucial for interpretation of paleo-data, as many cores off the Pearl River mouth are being used for monsoon reconstruction.

Similar to the wind and current patterns, SST data also clearly show a cross basin, thermal front in winter (roughly along the 25.5 isotherm in Fig. 2.9A), albeit it often disappears in summer (Fig. 2.9B). This upper layer thermohaline front runs across the SCS basin from the South Vietnam coast to Luzon Island. The strength of the front is around 1 °C/100 km at the surface and 1.4 °C/100 km at the subsurface (−50 m) (Chu and Wang 2003). Accordingly, water masses north and south of this front are different, with high temperature, low salinity water in the south and low

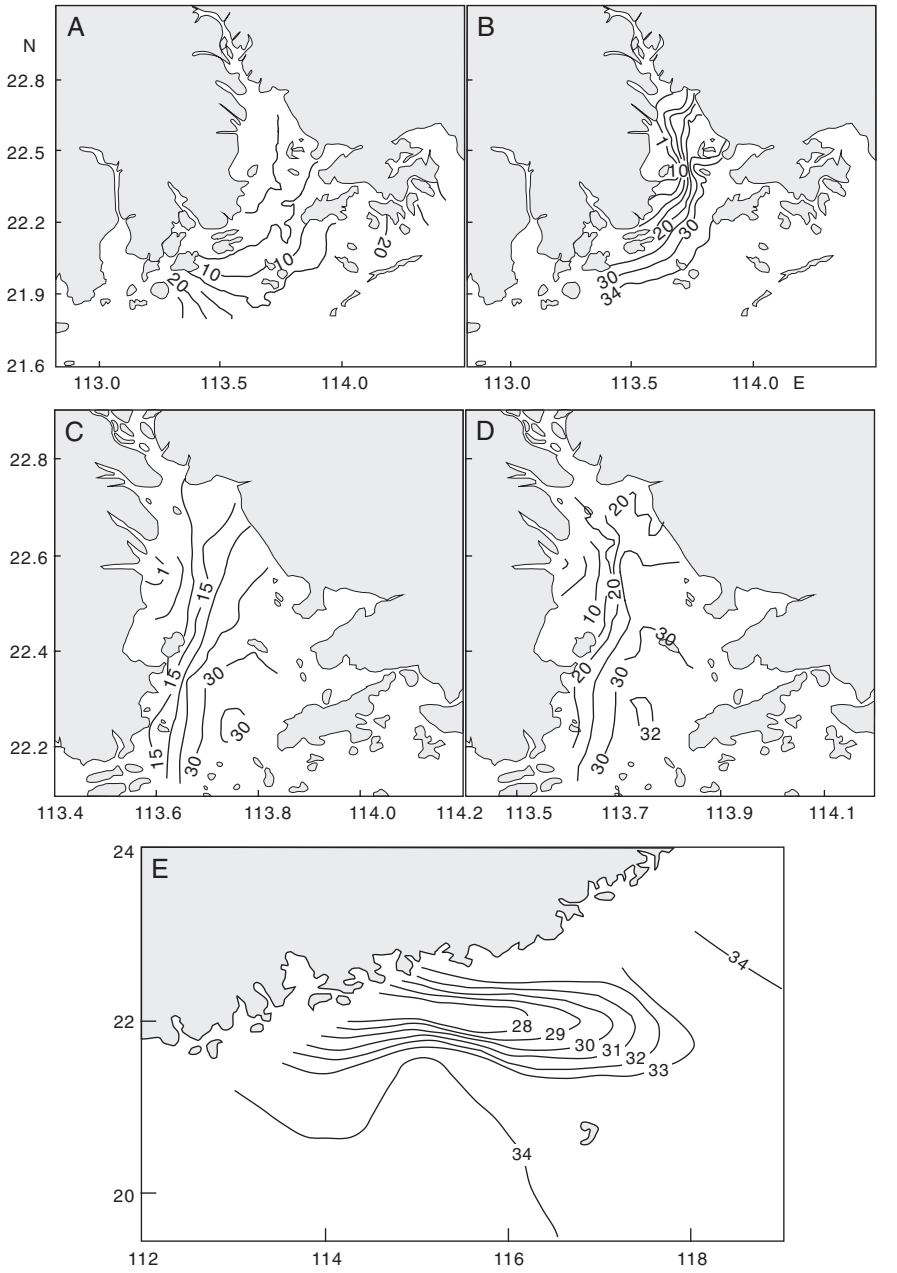

Fig. 2.10 Salinity distribution in the Pearl River estuary is shown by ‰ contours for July 1999 surface (**A**) and bottom (**B**) readings, for January 2000 surface (**C**) and bottom (**D**) readings (Dong et al. 2004), and (E) for June/July 1979 from sea surface outside the estuary (Su 2004)

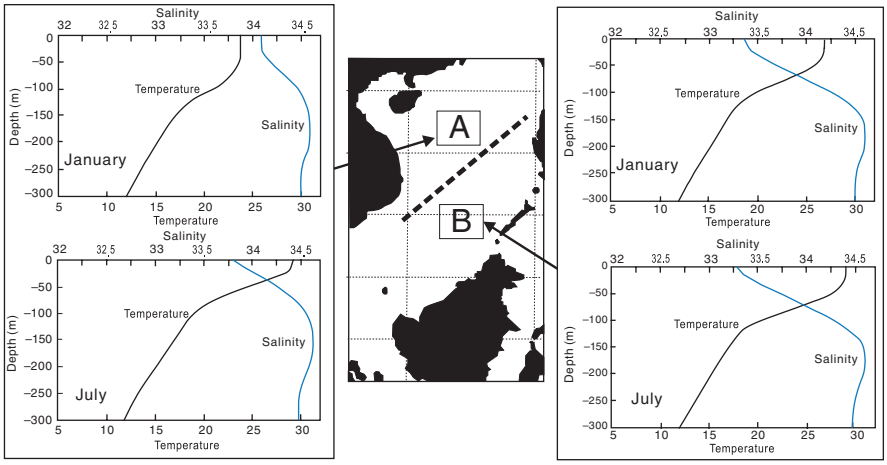

Fig. 2.11 January and July temperature and salinity profiles are compared across the thermohaline front (heavy dash line) between the northern (A) and southern (B) SCS (modified from Chu and Wang 2003)

temperature, high salinity water in the north, as seen clearly from a comparison of the upper layer (0–300 m deep) *T-S* diagrams between the northern and southern SCS shown in Fig. 2.11. Both the temperature and salinity curves show a larger range south of the front than to the north, and the salinity minimum in the north of the front occurs at a shallower depth than in the south. Thus, the thermohaline variability to the south is larger than to the north of the cross-basin current (Fig. 2.11).

Thermocline and Upwelling

In the SCS, a seasonal thermocline exists throughout the year in the deep basin. The thermocline layer is thinnest (< 100 m) in winter in most of the basin, thickest (∼150 m) in spring, and transitional in summer and autumn (100–120 m). The average thermocline depth is about 100 m in winter, ∼75 m in spring, 75–85 m in summer and autumn with a west-east difference of over 50 m (Fig. 2.12). The thermocline slope in the deep sea in winter is opposite to that in summer due to monsoon influence. The upper water piles up in the northwestern part of the SCS in winter and in the southeastern part in summer (Shaw et al. 1996; Liu Q. et al. 2000).

Similarly, the layer above the thermocline, or the mixed layer, varies in depth and in temperature under monsoon influence. In winter, it is thickest (∼80 m) in the NW part, becoming thinner in the south (∼40 m; Fig. 2.13A). In spring, the mixed layer decreased to about 30 m because of the weakened wind flow

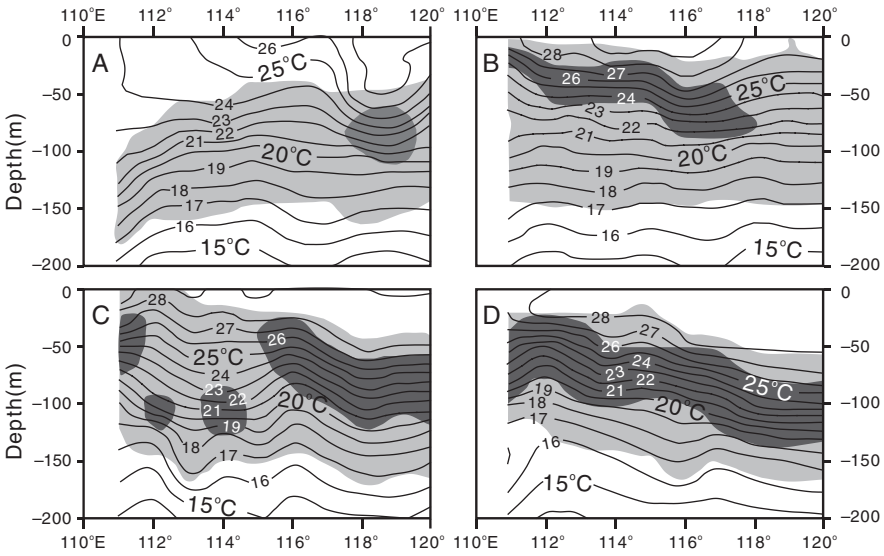

Fig. 2.12 Temperature-depth profiles across the SCS from NW (18 °N, 110 °E) to SE (12 °N, 120°E) are shown for (**A**) winter, (**B**) spring, (**C**) summer, and (**D**) autumn. Areas with vertical gradient >0.05 °C/m are lightly shaded, and those >0.1 °C/m heavily shaded (Liu Q. et al. 2000)

(Fig. 2.13B). In summer, the mixed layer pattern is opposite to that in winter, becoming thicker in the south (∼50 m) and thinner in the northwest (∼30 m; Fig. 2.13C). The mixed layer in autumn is relatively thick over the entire SCS basin (∼50 m), becoming slightly thinner only off the Vietnam coast (∼40 m; Fig. 2.13D) (Shi et al. 2001).

The southern coast of Vietnam is oriented in a SW-NE direction, roughly in parallel with the prevailing southwesterly winds in summer. Due to the Ekman principle, the alongshore wind can easily pump cold waters from beneath the mixed layer to the surface at such a setting, causing the maximum offshore cooling to concur approximately with the summer wind speed maximum along the coast (Xie et al. 2003). A similar phenomenon occurs in winter in the northeast SCS off Luzon, where coastal upwelling is driven by northeasterly monsoon winds. Therefore, two primary regions of deep upwelling exist corresponding to the two eddies in Fig. 2.7A: west of Luzon and east of Vietnam. The winter Luzon cold eddy and the summer Vietnam cold eddy can be easily recognized from the upper layer temperature distribution (Yang and Liu 1998). From October to December, shelf break upwelling along the edge of Sunda Shelf may also occur (Chao et al. 1996).

The development of monsoon-induced upwelling can be better demonstrated using satellite data. It was found, for example, that the summer southwesterly winds impinge on mountain range on the Vietnam eastern coast, and a strong wind jet occurs at the southern tip offshore of Vietnam, resulting in strong wind curls that are

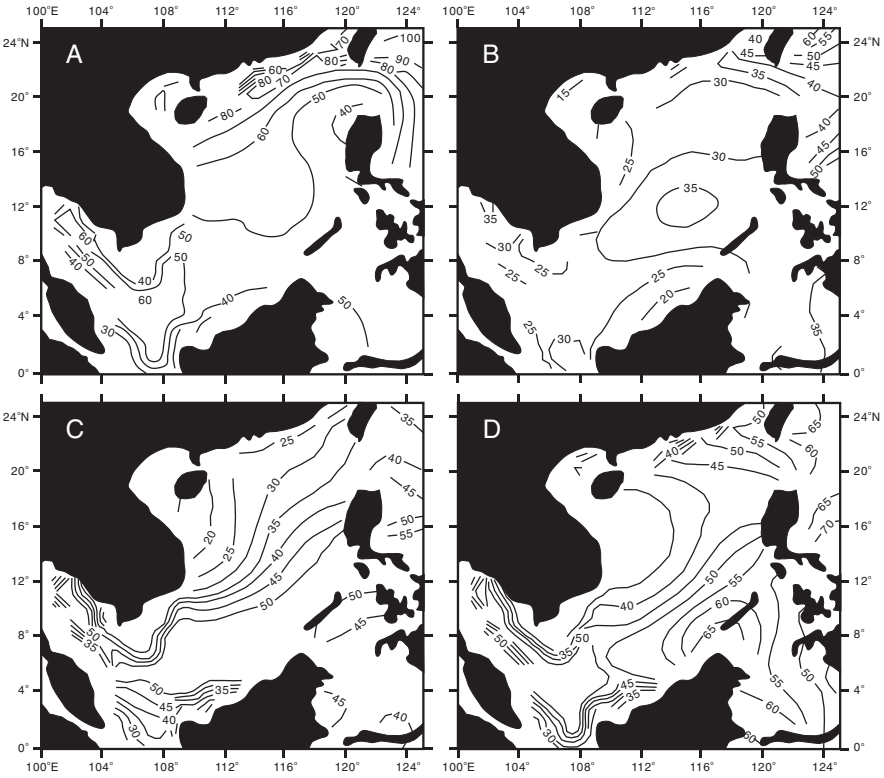

Fig. 2.13 Maps show the mixed layer depth in the SCS in (**A**) January, (**B**) April, (**C**) July, and (**D**) October (Shi et al. 2001)

responsible for upwelling off the coast. In July and August an anticyclonic ocean eddy develops to the southeast, advecting the cold coastal water offshore into the open SCS (Fig. 2.14A). Ocean color observations also revealed a collocated tongue of high chlorophyll concentration in the area (Fig. 2.14B). However, cold water extending to the east in this area is subject to interannual variations. In 1998, when monsoon winds weakened during the El Niño year, this cold water tongue and mid-summer cooling never took place (Xie et al. 2003). Aside from monsoons, tropical cyclones are frequent in the SCS, averaging to 10 typhoons per annum. Tropical cyclones traverse the SCS, also causing upwelling of cold subsurface water into the mixed layer (Wong et al. 2007a).

Water Exchange with Pacific and Kuroshio Intrusion

Only the surface waters in the SCS exchange freely with those in the neighboring seas, while deeper waters flowing into the SCS are primarily from the western

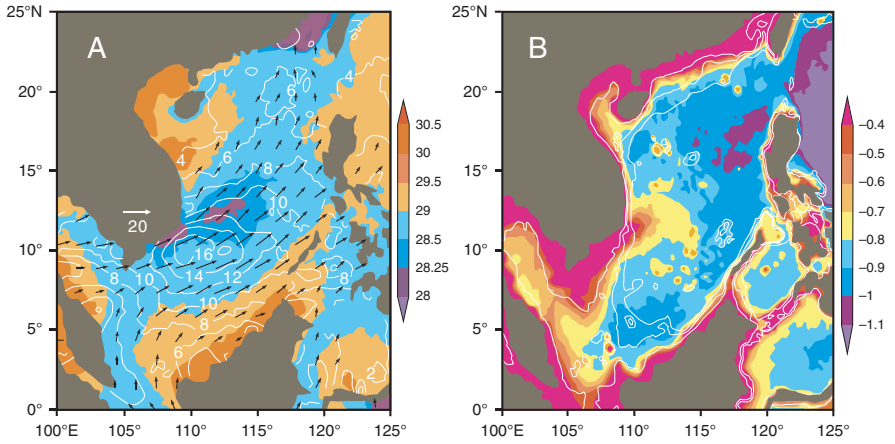

Fig. 2.14 Summer upwelling off Vietnam coast is shown with (**A**) AVHRR August sea surface temperature (color shade in °C) and QuikSCAT surface wind vectors and magnitude (contours in 10^{-2}Nm^{-2}), and (**B**) log^{10} of SeaWiFS chlorophyll concentration averaged for July–August 1999–2002 (color shade in mg/m^3), with bottom isobaths for 50 m, 100 m and 500 m, respectively (Xie et al. 2003)

Philippine Sea through the Bashi Strait. The Tropical Water, originating from the high-salinity pool in the subtropical North Pacific, occurs as a salinity maximum at around 150 m in the SCS. The North Pacific Intermediate Water, flowing from the subpolar North Pacific, occurs as a salinity minimum centered around 500 m. As the Bashi Strait with its sill depth of 2,400 m is the only deep water connection with the Pacific, deep water in the western Philippine Sea overflows the sill and fills the deep SCS (Table 2.2). The water transport through the Bashi Strait influences the circulation and heat budget of the SCS, and determines the nature of its deep water. The annual water budget of the SCS is summarized in Table 2.3.

Wyrtki (1961) was the first to note that waters enter the SCS in winter and flow back to the Pacific in summer. It is now generally accepted that the Bashi Strait transport has a sandwiched vertical structure, with the Philippine Sea water entering the SCS at the surface and in the deeper parts, and with the net Bashi Strait transport out of the SCS at intermediate depths. The net transport of the western Pacific water into the SCS is estimated at the order of 4 Sv by Qu et al. (2000) or in a range of

Table 2.2 Properties of water masses at different depth intervals at the SEATS station (18.3 °N and 115.5 °E), northern SCS (data from Wong et al. 2007b)

	Tropical water	North Pacific Intermediate Water (upper)		Deep water	
Depth (m)	100–150	470–500	1,500–1,600	2,400–2,700	2,800–3,000
Potential T (°C)	16.2–22.1	7.5–10.2	2.60–2.91	2.16–2.20	2.11–2.14
Salinity (‰)	34.56–34.72	34.40–34.42	34.57–34.61	34.59–34.62	34.60–34.63

Table 2.3 Characteristics of annual water budget of the SCS show variations in input and output volumes (modified from Wong et al. 2007a)

Input	Flux (km^3/year)	Output	Flux (km^3/year)
Surface inflow from western Philippine Sea	2.7×10^{-1}	Surface outflow to western Philippine Sea	-2.4×10^{-1}
Deep water inflow from western Philippine Sea	3.7×10^{-2}	Net outflow at upper intermediate depths to W Philippine Sea	-5.8×10^{-2}
Surface inflow from Sulu Sea	1.8×10^{-2}	Net surface outflow to Java Sea	-1.8×10^{-2}
Riverine input	1.7×10^{-3}	Surface outflow to East China Sea	-1.1×10^{-2}
Net precipitation	2.5×10^{-3}		

4.2–5.0 Sv by Su (2004). In any case, the SCS plays the role of a "mixing mill" that mixes surface and deep waters from the western Pacific and returns them through the Bashi Strait at upper intermediate depths (Yuan 2002).

Water transport through the Bashi Strait can be illustrated with results from a field experiment in October, 2005. The distribution of the subinertial flow not only displays different directions between the upper, middle and lower layers, but also a north-south contrast (Fig. 2.15). The results from this experiment also show that the net volume of westward transport is 9 Sv in the upper layer (< 500 m) and 2 Sv in the deep layer ($> 1,500$ m), and the net volume of eastward transport in the intermediate layer (500–1,500 m) is 5 Sv (Tian J.W. et al. 2006).

A more controversial issue is Kuroshio intrusion. As the subtropical west boundary current in the North Pacific, the Kuroshio forms in the east of the Philippines around 13 °N and flows north along the coast of Luzon and, after making a slight excursion into the Bashi Strait, continues northward east of Taiwan. A variety of models have been proposed about how the Kuroshio water invades the SCS. Earlier studies suggested that the Kuroshio could loop around inside the SCS or even intrude as a direct current, but the suggested flow patterns have not been confirmed by any synoptic surveys (Su 2004). However, most numerical models with open boundaries predicted a loop current and a branch current, both from the Kuroshio, into the SCS (e.g., Yuan 2002; Metzger and Hurlburt 1996, 2001). Some authors go even further to believe that impingement of the intruded Kuroshio with the continental margin in the SCS may bring about a SCS Warm Current, which flows northeastward in waters down to 200–400 m along the shelf break from southeast of Hainan Island to the southern end of Taiwan (Guan 1985; Hsueh and Zhong 2004).

The discrepancy between the modeled and observed flow patterns may have been caused by insufficient resolution of topographic features from the Bashi Strait for modeling and by inability of the models to properly represent the physics of Kuroshio intrusion. As Su (2004) argues, a steady branch current from the Kuroshio to the west through the Bashi Strait is physically impossible, and the only possibility for a part of the Kuroshio water to flow through the Strait is via

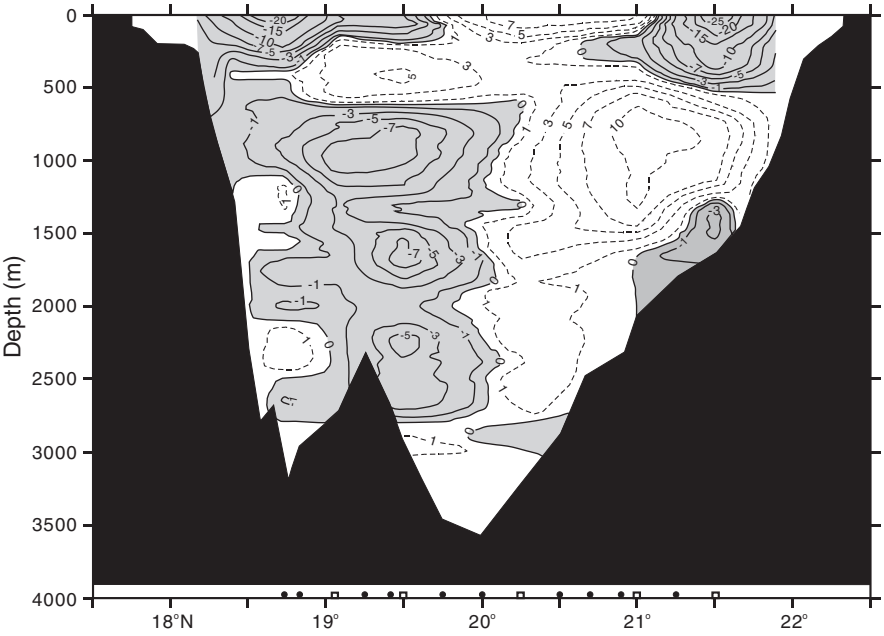

Fig. 2.15 A cross section shows subintertial flow velocity (cm/s) across the Bashi Strait. Dashed lines and positive values denote the eastward flow, solid lines and negative values denote the westward flow (also *shaded gray*). The topography is shaded black (Tian J.W. et al. 2006)

submeso-scale processes such as eddies. Once generated in the Bashi Strait, these submeso-scale eddies will propagate to the west, resulting in a net flow to the SCS. Such an influx is likely from the Kuroshio frontal water rather than its proper water, and the frontal water has hydrographic characteristics close to the SCS water (Su 2004).

Regardless of all the controversy and complexity, the Kuroshio water does enter the SCS one way or another and exchanges with the SCS water through the Bashi Strait. Cumulatively, there is a small (∼1 Sv) net outflow of surface water (0–350 m depth) from the SCS in the wet season, but a net inflow (∼3 Sv) in the dry season through the Bashi Strait. The differences are mainly made up by inflow and outflow of Sunda Shelf Water in the wet and dry seasons, respectively. Below 350 m, the SCS water flows out, but the West Philippine water again flows into the SCS below 2,500 m, making the deep SCS waters homogenous with the same property as the Philippine Sea (Chen and Huang 1996). In general, a mass balance of inflowing deep waters from the western Philippine Sea is maintained primarily by upwelling and mixing with shallower waters in the SCS and an outflow at intermediate depths to the western Philippine Sea through the Bashi Strait. A rigorous exchange of water between the SCS and the western Philippine Sea has resulted in a residence time of the deep water in the SCS as short as 30–150 years, and the corresponding basin-wide upwelling rate should be as high as about 10–90 m/yr. Such a high upwelling

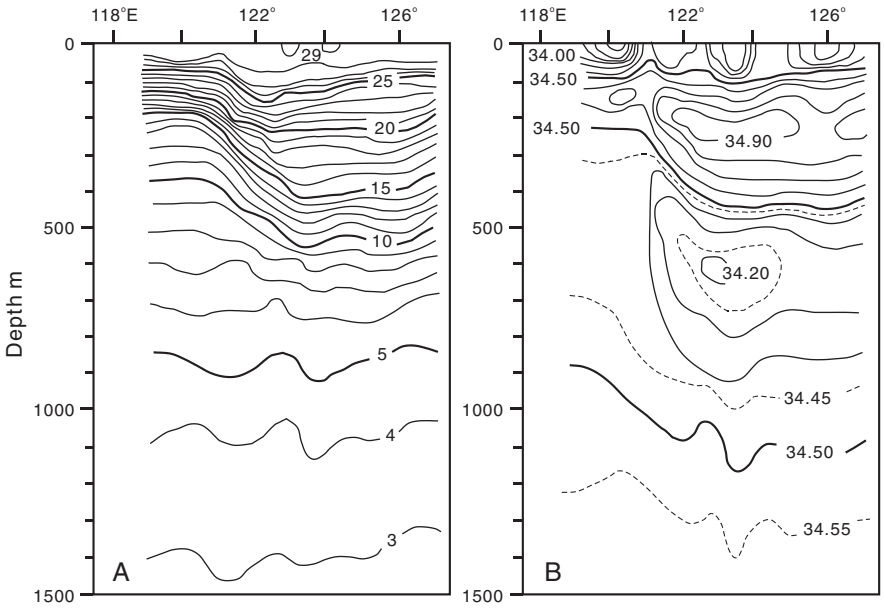

Fig. 2.16 Profiles show variations along 19.5 °N in (**A**) temperature (°C) and (**B**) salinity (‰) across the Bashi Strait (at ~122 °E) in summer 1965 (from Su 2004 after Nitani 1972)

rate gives rise to a thin mixed layer and a shallow top of the nutricline in the SCS (Wong et al. 2007a).

All these result in significant difference in the vertical structure of waters between the two sides of the Bashi Strait. Fig. 2.16 shows the temperature and salinity distribution in the water column across the Strait. In the Philippine Sea, the salinity maximum layer is related to the North Pacific Tropical Water (NPTW), and the salinity minimum to the North Pacific Intermediate Water (NPIW). After crossing the Strait, both salinity maximum and minimum weaken significantly (Fig. 2.16B). Furthermore, the temperature and salinity contours above 600 m shoal up by about 50–200 m to the west, with a continuous shoaling of the salinity contours to about 1,000 m. Thus, at the same depth in the upper 600 m of the ocean, the SCS water is cooler than the western Philippine Sea water. The thickness of the mixed layer in the SCS is also only about half that of the western Philippine Sea. Such apparent "upwelling" hydrographic features in the upper 600 m of water are found over the entire deep basin of the SCS. Below about 600 m, the SCS water becomes slightly warmer than the Philippine Sea water (Su 2004).

The water columns from the two sides of the Bashi Strait differ also in biogeochemistry. The subsurface water of the SCS west of Luzon is more enriched in nutrients and depleted in oxygen relative to the water east of the Strait, but the situation reverses in the intermediate water (Gong et al. 1992). Comparison between dissolved oxygen concentrations at different depth intervals in the Pacific side of the Strait clearly reveals this feature. Specifically, the oxygen content is higher

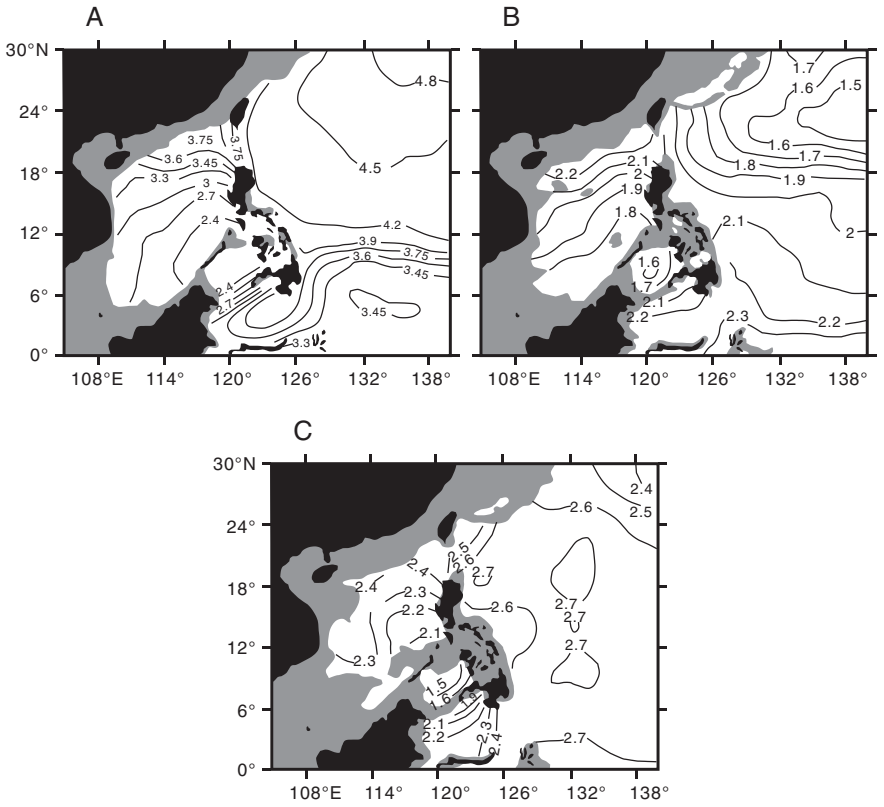

Fig. 2.17 Maps show variations of dissolved oxygen concentration (ml/l) at (**A**) 140 m, (**B**) 1,000 m and (**C**) 2,000 m water depths in the western Pacific on both sides of the Bashi Strait. Note a relative high level in intermediate waters of the SCS compared to other marginal sea basins (Qu 2002)

above 600–700 m, lower between 700 and 1,500 m, then higher again below 1,500 m (Fig. 2.17) (Qu 2002).

Deep Water Circulation

Deep waters in the western Pacific marginal seas, such as the SCS and Sea of Japan, are uniform in properties but different in their origins. In the Sea of Japan, the dense deep water is formed in its northern half under low temperature, whereas in the SCS all waters below 2,000 m are of Pacific origin and have the same hydrographic properties as western Pacific water at about 2,000 m (Su 2004). The incoming Pacific water crosses the Bashi Strait, sinks, spreads out, and fills the SCS deep basin. As a result, the potential temperature in the SCS is above 2.1 °C even at 4,000 m, almost 0.8 °C warmer than in the western Pacific at the same depth (Chen C. et al. 2001).

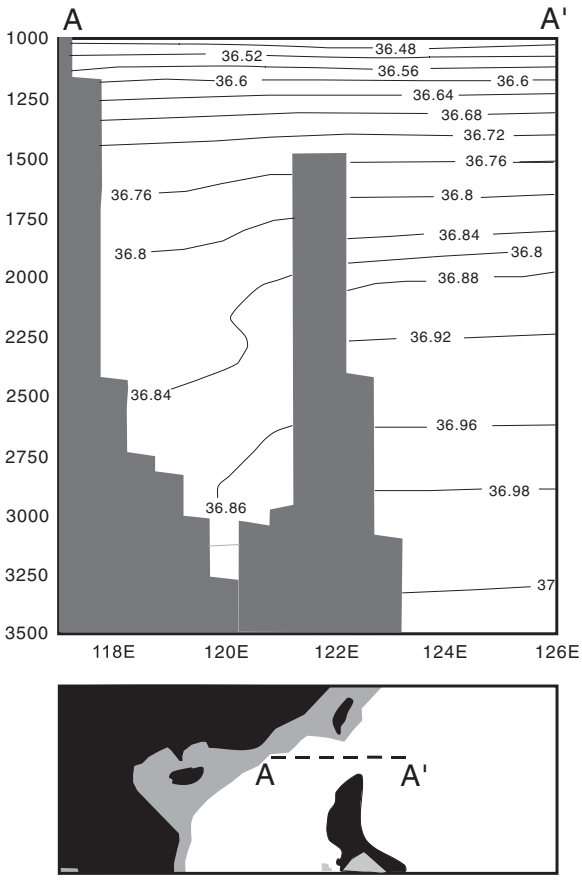

Fig. 2.18 Profile of potential density (kg/m^3) is shown along 20 °N, across the Bashi Strait. Bottom topography (*shaded*) is on the 0.5° grid and does not represent the actual water depth range (Qu et al. 2006)

Across the Bashi Strait, a persistent density difference exists between the Pacific and the SCS (Fig. 2.18). Water on the Pacific side is well stratified, with potential density increasing from about 36.48 kg/m^3 at 1,000 m to 37.00 kg/m^3 at 3,500 m. No deepwater stratification is obvious on the SCS side, where water density is vertically uniform with a density range of only about 0.02 kg/m^3 below 2,000 m (Fig. 2.18) (Qu et al. 2006).

Up to now, there is virtually no direct observation indicative of any distribution route of the Pacific water into the deep SCS. However, the density field based on the synthetic salinity data (Fig. 2.19A–C) may throw some light on the deep SCS circulation. Upon entering the SCS through the Bashi Strait, waters of Pacific origin first turn northwestward and then southwestward along the continental margins off southeast China and east Vietnam. This suggests that the deep-layer circulation in the SCS is predominantly cyclonic. The intrusion of deep Pacific water is also evident in oxygen distribution used as a passive tracer (Fig. 2.19D). As it spreads over the SCS, water from the Pacific gradually gets mixed with ambient

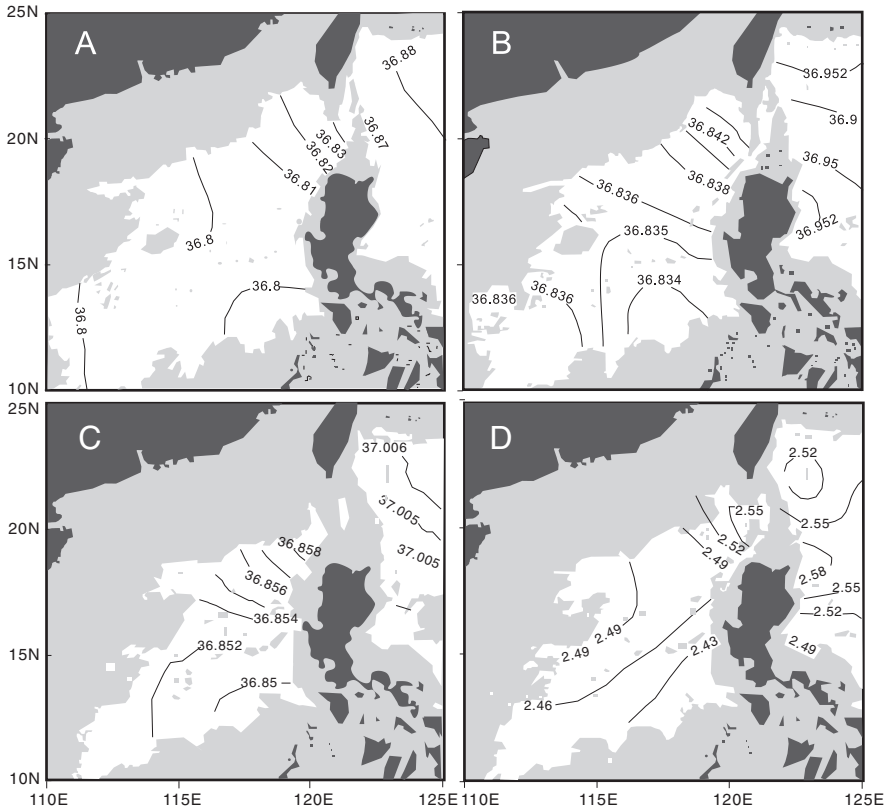

Fig. 2.19 Potential density in kg/m^3 is calculated from the synthetic salinity depths at (**A**) 2,000 m, (**B**) 2,500 m and (**C**) 3,500 m, while (**D**) shows dissolved oxygen concentration (mL/L) along 36.84 density surface, lying at depths roughly between 2,000 and 3,000 m (Qu et al. 2006)

waters, loses its Pacific characteristics, and returns in less dense layers. Therefore, density distributions within the sea basin suggest a cyclonic deep boundary current system, as might be expected for an overflow-driven abyssal circulation (Qu et al. 2006).

Thus, the abyssal basin of the SCS is filled constantly by the Pacific water flowing down the sill of the Bashi Strait, and the deep SCS water is believed to upwell into the intermediate SCS water between 350 and 1,350 m, which is then exported out of the SCS again through the Bashi Strait (Su 2004). The deep SCS water was estimated to have a fast flushing time of 40–50 years (Chen C. et al. 2001) or even less than 30 years (Qu et al. 2006). Therefore, the intermediate, deep and bottom waters are essentially the same age. Because of a short residence time, the amount of particulate matter decomposition in the water column is sufficient to produce only a small maximum of chemical properties in the vertical profiles (Chen C. et al. 2001).

Other Oceanographic Features

Recent studies in the SCS have discovered a number of new oceanographic features which are not yet attended to by geologists but certainly are of potential significance for studies of paleoceanography and sedimentology. Two of these features, namely the inner waves and meso-scale eddies, are very briefly discussed here.

The Bashi Strait is important not only because of its role in water exchanges between the SCS and the Pacific but also as the source region of internal waves observed in the northern SCS. Internal waves can be recognized using synthetic aperture radar (SAR) satellite images. Most SAR images of the northern SCS show nonlinear internal waves (Hsu et al. 2000), from west of Bashi Strait to east of Hainan Island (Liu A. et al. 1998). Generally, the tidal flow over topographic features such as a sill or continental shelf in a stratified ocean can produce nonlinear internal waves. Recent observations in the northeastern SCS show that non-linear internal waves emanate nearly daily from the Bashi Strait during spring tide and rapidly propagate westward to the shallow region west of 118 °E. The amplitude of these waves reach 140 m or more, forming the largest free propagating nonlinear internal waves observed in the internal basin. Their propagation speed at about 2.9 m/s is also faster than similar waves previously observed in the world's oceans. The most likely source region of these giant internal waves is the near 2,000-m-deep ridge in the northern Bashi Strait (Liu C. et al. 2006). These internal waves energize the top 1,500 m of the water column and move large amounts of nutrient up, and their role in enhancing surface productivity and disturbing sedimentation may provide a highly interesting topic for research.

Meso-scale variability has been reported since the 1990s. The upper layer circulation of the SCS is characterized by basin-wide gyres, but embedded in the gyres are many meso-scale eddies, as observed from both hydrographic and altimeter measurements. Altimeter data over the SCS for 5 years from 1992 to 1997 reveal significant meso-scale variability mainly in two narrow strips north of 10 °N: one near the 2,000 m isobath over the NE slope and another as a SW-NE strip of about 450 km wide extending from Luzon to Vietnam (Wang L. et al. 2000). An 8-year time series of satellites data (1993–2000) shows that meso-scale eddies are a constant feature in the SCS, basically in all areas deeper than 2,000 m. Altogether 58 anticyclonic eddies and 28 cyclonic eddies were identified for this period in the SCS, and a typical eddy has a lifetime of about 130 days and a diameter of 300 km. Likely mechanisms causing these eddies include Kuroshio intrusion in SW of Taiwan, vorticity advection from the Kuroshio, Kuroshio-Island interaction, the eastward baroclinic jet off Vietnam and the intense wind-stress curl northwest off Luzon (Wang G. et al. 2003).

Oceanographic Summary

To sum up, the modern oceanography of the SCS is distinguished by the following major features which are highly relevant to interpreting geological records:

1. *Seasonality*. Despite its low-latitude position, the SCS shows strong seasonal variations in water circulation and composition. Driven by East Asian monsoons, the surface circulation is characterized by seasonally alternating basin-scale gyres. Water exchanges with the Pacific and CO_2 exchange with the atmosphere (Chapter 7) are also subject to remarkable seasonal variations. Monsoon winds drive the thermocline to tilt up from NW to SE in winter but tilt to opposite direction in summer. Two coastal upwelling areas are associated with monsoons: west of Luzon in winter and east of Vietnam in summer. Unlike the Indian monsoon, the local winter monsoon exceeds the summer monsoon in strength and in time duration on a yearly basis. Therefore, it is unwise for SCS studies to indiscriminately copy monsoon proxies or climate cyclicity from other regions.
2. *North-South contrast*. The SCS basin is oceanographically dividable into two halves by the monsoon wind jet and the cross-basin current axis in a NE-SW direction, which is associated also with the upper layer thermohaline front. The northern part is controlled by the monsoon-driven cyclonic gyre, while the southern part belongs in the Western Pacific Warm Pool with much less monsoon influence. Accordingly, the northern SCS is distinguished from its southern counterpart by higher salinity and lower temperature. In the past, this N-S contrast became intensified with the growth of the boreal ice sheet and the strengthening of the winter monsoon. Topographical and geological contrasts between the landward side to the northwest and the island arc side to the southeast also enhance many sedimentological and paleogeographic differences between the southern and northern SCS.
3. *Basin-wide upwelling*. The modern SCS exchanges with the open western Pacific, i.e., the western Philippine Sea, through the Bashi Strait with a sill depth of $\sim 2,400$ m. Originated from the western Philippine Sea, deep waters in the SCS are relatively uniform below 2,000 m. The deep water inflow results in an estuarine basin-wide upwelling, a shorter residence time, and a shallower thermocline in the SCS than in the open ocean, making the upper water structure and productivity in the SCS more sensitive to monsoon variations.

2.3 Tectonic History and Sedimentary Basins

The tectonic history of the South China Sea (SCS) was genetically related to the deformation of Asia. After India-Asia collision in the Eocene, Asia significantly enlarged its size and increased its altitude. The west-tilting topography of East Asia was reversed with uplift of the Tibetan Plateau and opening of marginal seas, including the SCS (Wang P. 2004). Separated by continental fragments, these marginal sea basins formed as a result of long-lasting extension along the southern margin of mainland Asia (Taylor and Hayes 1980; Holloway 1982) (Fig. 2.20).

Tectonically, the SCS is bounded by the South China (Yangzi) Block in the north, by the Indochina Block in the west, by the Philippine Sea Plate in the east, and in

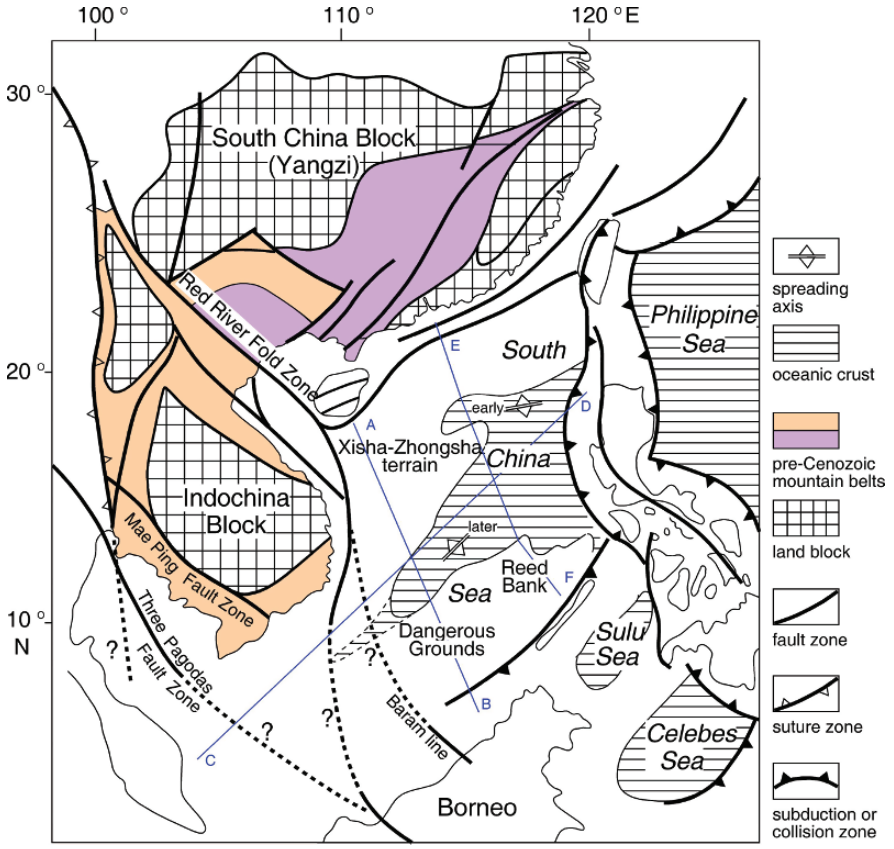

Fig. 2.20 Map shows land blocks and major fault systems surrounding the SCS (modified from Gong and Li 1997; Hall 2002; Pubellier and Chan 2006). Lines A-B, C-D and E-F are locations for sections shown in Fig. 2.22

the south by Borneo Island and the Indonesian Archipelago (Fig. 2.20). This unique setting not only directly controls the general development of the SCS and its basins but also makes it unique in having its own spreading axis among the western Pacific marginal seas.

Up to now, however, no consensus has been reached on the mechanism of the SCS formation (Fig. 2.21). Hypotheses currently gaining relative wider acceptance include (1) India-Eurasia continental collision and the collision-resultant tectonic extrusion process mainly along the Red River Fault Zone (RRFZ), or Ailao Shan-Red River (ASRR) shear zone (Taylor and Hayes 1980, 1983; Tapponnier et al. 1982, 1986; Briais et al. 1993; Lee and Lawver 1994; Zhou et al. 1995), (2) the extensional force from subduction processes of the Pacific Plate along the western Pacific margin (Hawkins et al. 1990; Stern et al. 1990; Hall 2002) (Fig. 2.21), and (3) the extensional force from an upwelling mantle plume (e.g., Zhu and Wang 1989; Fan and Menzies 1992) or movement of the upper asthenosphere

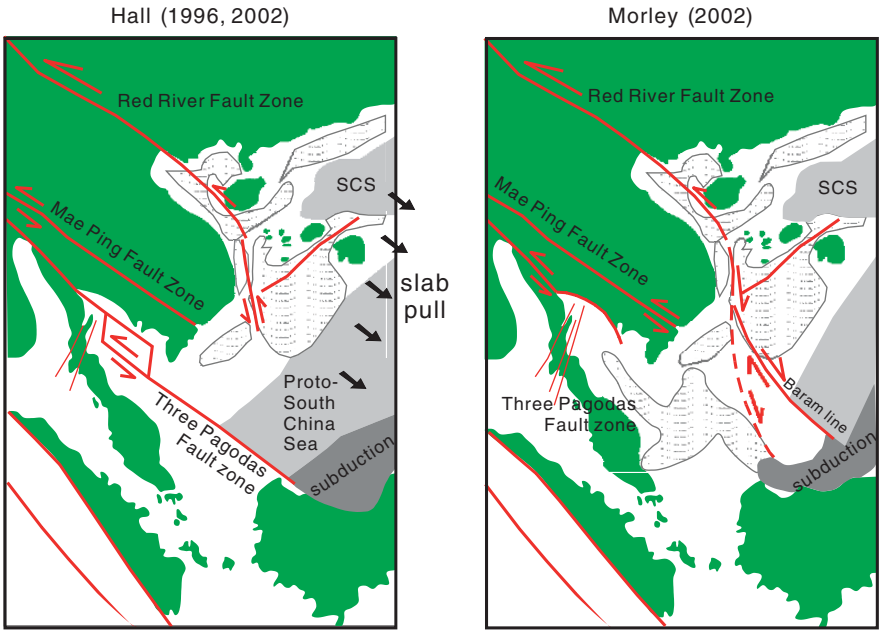

Fig. 2.21 Models show the important role of the Red River Fault Zone and other fault systems for the opening of the SCS (modified from Morley 2002 and Hall 2002). Also shown is the outline of major sedimentary basins and the Proto-South China Sea

(Yao 1996; Yao et al. 2005). It may not be ruled out, however, that a combined process of the above probable driving forces has been in operation especially when the regional tectonic regime changed dramatically after collision between Indo-Australian and Eurasian and Pacific plates became intensified since the Eocene (Hall 2002; Pubellier et al. 2004), as implied also by modeling results (Xia et al. 2006). In this section, we provide a brief account on the tectonic history of the South China Sea and its sedimentary basins.

Prior Terrains and Opening of the SCS

Deep seismic surveys indicate a continental crust thinning from 30 to 35 km along the northern continental margin to ~14 km under the lower slope of the SCS, while the depth of Moho under the deep central basin is generally < 12 km (Nissen et al. 1995; Gong and Li 1997; Yan et al. 2001; Hutchison 2004) (Fig. 2.22). As a failed rift structure, for example, the Xisha Trough between Hainan and Xisha (Paracel) islands has a very thin continental crust of only 8 km with little magmatic underplate in the lower crust (Qiu et al. 2001). A relative thin crust of 8–12 km exists also in the northeast end, between Taiwan and Dongsha Rise (Yeh and Hsu 2004). Hayes and Nissen (2005) modeled the crust thickness and found that crustal extension

was much less in the east than in the west where the thermal structure of pre-rift lithosphere was by a factor of two prone to rifting.

Pre-Cenozoic rock types known to occur in the SCS include Jurassic to Cretaceous marine shale and sandstone and Cretaceous or older igneous granite, as well as metamorphic rocks. Overall, igneous rocks may constitute 50% or more of the prior terrains, some of which remain as structural highs in the subsequent basin formation. Around the central deep basin, numerous coral reefs developed on terrain systems including the Nansha Terrain (Reed Bank and Dangerous Grounds) and the Xisha-Zhongsha Terrain (Paracel Island and Macclesfield Bank). Now lying in the south, the Dangerous Grounds, Reed Bank, Nansha (NW Borneo) Trough and Palawan Island were originally terrains of continental origin. They were rifted southward in the late Cretaceous-early Paleogene and later, during the course of seafloor spreading, their edge collided with the northernmost terrain of the proto-Sulu Sea (Schlüter et al. 1996). In the south, apart from granite and dorite, volcanic and shallow marine sediments are also common, indicating a more complex pre-rift lithotopography (ASCOPE 1981; Du Bois 1985).

Wider occurrence of Jurassic and Cretaceous marine shale and sandstone indicates a broad shallow "Proto-South China Sea" during the late Mesozoic to early Cenozoic probably with some deep troughs connecting to the eastern Indian Ocean (e.g., Hall 2002) (Fig. 2.21). This "Proto-SCS" has since been largely subducted into, or uplifted as part of, the southeastern island arcs. The total Mesozoic sequence may reach a maximum thickness of about 2,000–4,000 m (Jin 1989; Xia and Zhou 1993), often with high magnetization on uplifted highs and low magnetization in basins (Li C. et al. 2008).

Initial rifting and graben-forming in the SCS region coincided with the early stage of Indian/Eurasian collision during the Paleocene-early Eocene, which became intensified from about 50 Ma (Harrison et al. 1992; Copeland 1997) (Fig. 2.23). Recent investigations of seismic and provenance data from the Indus Fan region indicate an earlier intensification period from about 55 Ma (Clift et al. 2001). However, it was not until the latest Eocene-earliest Oligocene when the collision-subduction-uplift process became powerful enough to substantiate any significant continental escape (Tapponnier et al. 2001) that ultimately contributed to rifting and spreading of the South China Sea. A total of ~550 km displacement of the Indochina subcontinent due to intensive strike-slip activities along the Red River Fault (Tapponnier et al. 1986; Briais et al. 1993; Leloup et al. 2001) during the Oligocene-Miocene may partly account for seafloor spreading in the SCS. In situ Th-Pb ion microprobe dating of monazite inclusions in garnets from the Red River Fault indicates that synkinematic garnet growth associated with left-lateral shearing between 34 Ma and 21 Ma in the northern region and sinistral deformation along the fault zone between 34 Ma and 17 Ma, confirming the close relationship between Indochina extrusion and SCS spreading (Gilley et al. 2003). Other forces involving in the opening of the SCS may include slab pull due to subduction of the Proto-SCS into the Philippine Sea Plate (Hall 2002; Hall and Morley 2004) (Figs. 2.21 and 2.23), similar to other SE Asian marginal seas due to subduction of the Indian-Australian Plate (Pubellier et al. 2003, 2004). The mechanism causing extensional

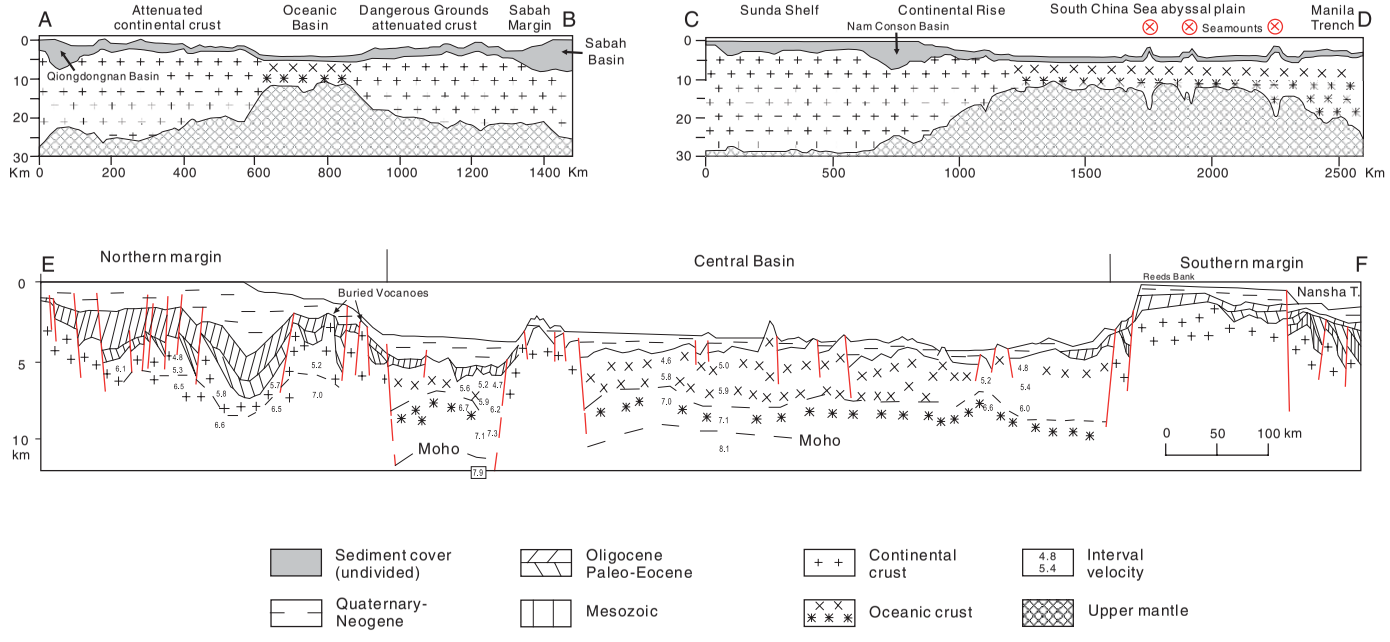

Fig. 2.22 Generalized crustal cross sections along lines A-B, C-D, and E-F (locations in Fig. 2.20) show variations in crust thickness and sediment cover in the SCS. Sections A-B and C-D are modified from Hutchison (2004), and section E-F from Yan et al. (2001). Note that scales are different

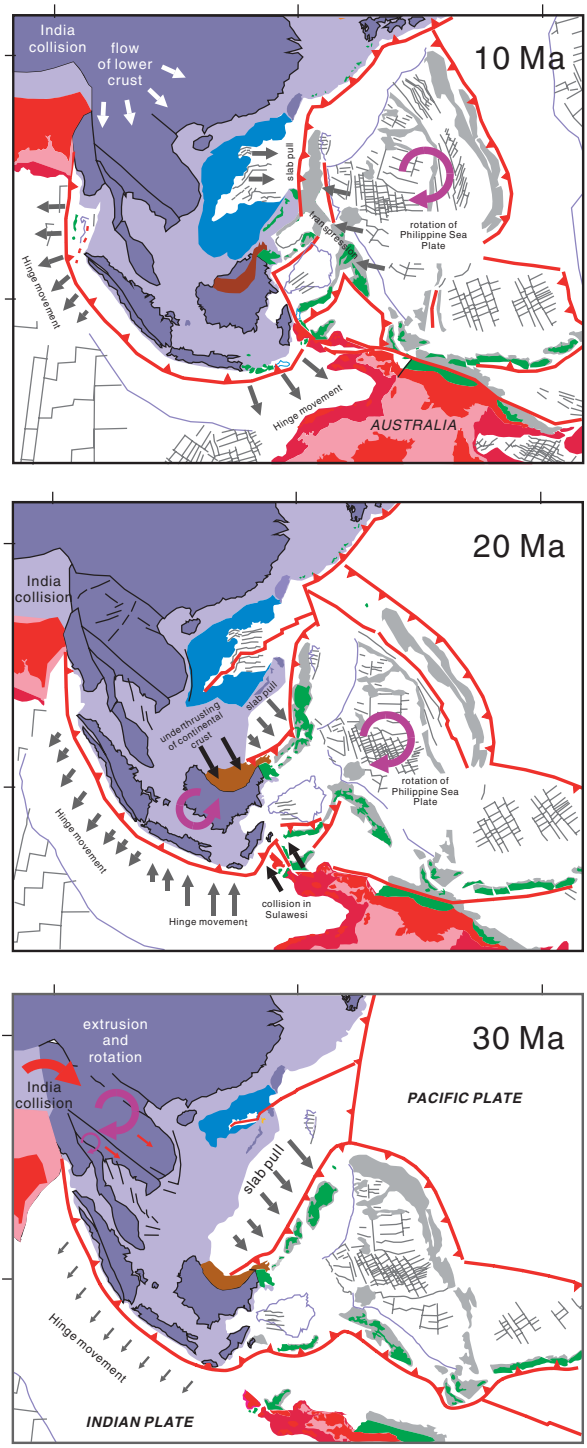

Fig. 2.23 Reconstruction maps for tectonic evolution in the SE Asian region at 30, 20 and 10 Ma show large scale movements of plates and land blocks (simplified from Hall and Morley 2004)

faulting and sea opening is extremely complex, and may have been influenced also by variations of slab dip structure in subduction zones (Lallemand et al. 2005).

Rifting started earlier in the north and northeast and appear to have been periodic during the Paleogene and, in some areas, the early Miocene (Taylor and Hayes 1980, 1983; Ru and Pigott 1986; Jin 1989; Sibuet et al. 2002, 2004). A recent compilation of GIS-based morpho-tectonic data for the northern SCS region has generated many digitized maps showing important fault systems, mountain ranges, and basins in various time periods (Pubellier et al. 2005; Pubellier and Chan 2006). Rifting in the western and southern parts occurred in the Eocene or later, implying two different tectonic and geomorphologic provinces between the then northern and southern + western SCS (Hayes and Nissen 2005). These two provinces show different lithofacies marking different early developing histories largely relating to different strike-slip faults in the SE along the so-called "Baram line", a proposed extension of the Red River Fault, as well as to local fault systems since the Eocene time (Morley 2002; Hayes and Nissen 2005) (Figs. 2.20 and 2.21).

Early studies of magnetic anomalies clearly reveal three important stages in the development of the SCS (Fig. 2.24). Seafloor spreading began at least from Chron 11 and ended at Subchron 5C (e.g., Briais et al. 1993), corresponding to the time

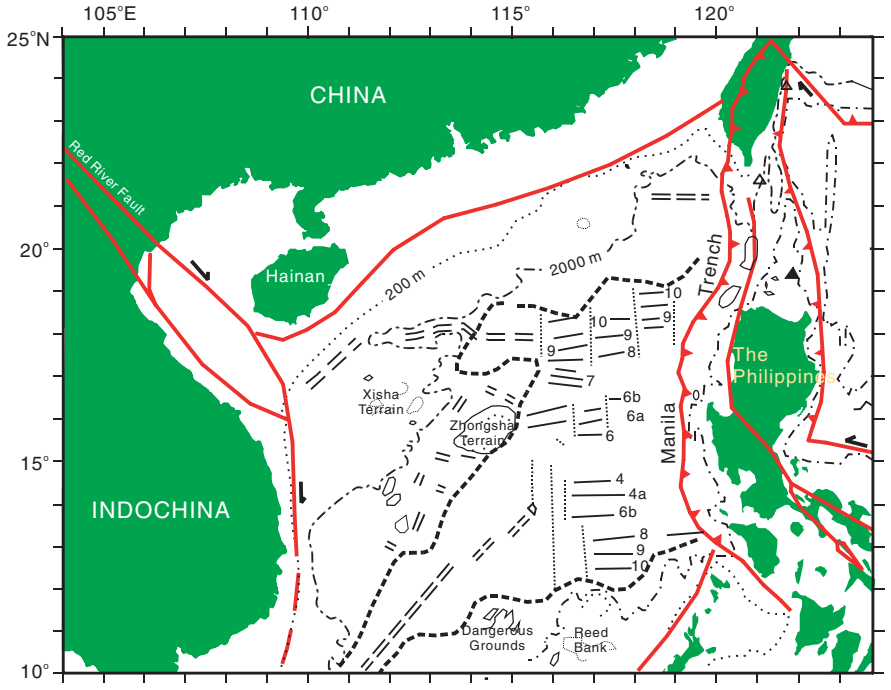

Fig. 2.24 Major tectonic elements of the northern and central parts of the SCS are shown with early interpretation of magnetic anomaly lineaments in the central deep basin as outlined by the thick dash line (modified from Hayes et al. 1995)

interval of 30–16.7 Ma using the new paleomagnetic time scale of Gradstein et al. (2004), or 32–16 Ma on older time scales. A southward ridge jump during the course of spreading occurred close to anomaly 7/6b boundary with an age of 23–25 Ma (old age 24–26 Ma), resulting in the separation of the Nansha from the Xisha-Zhongsha terrains (Fig. 2.24). However, because the igneous oceanic crust has not been drilled, there is no unanimity about the exact age of SCS spreading. For example, Barckhausen and Roeser (2004) argues that seafloor spreading in the SCS started at ~31 Ma (anomaly 12) and ended at ~20.5 Ma (anomaly 6A1), with a ridge jump at 25 Ma when a second spreading center also developed in the southwest.

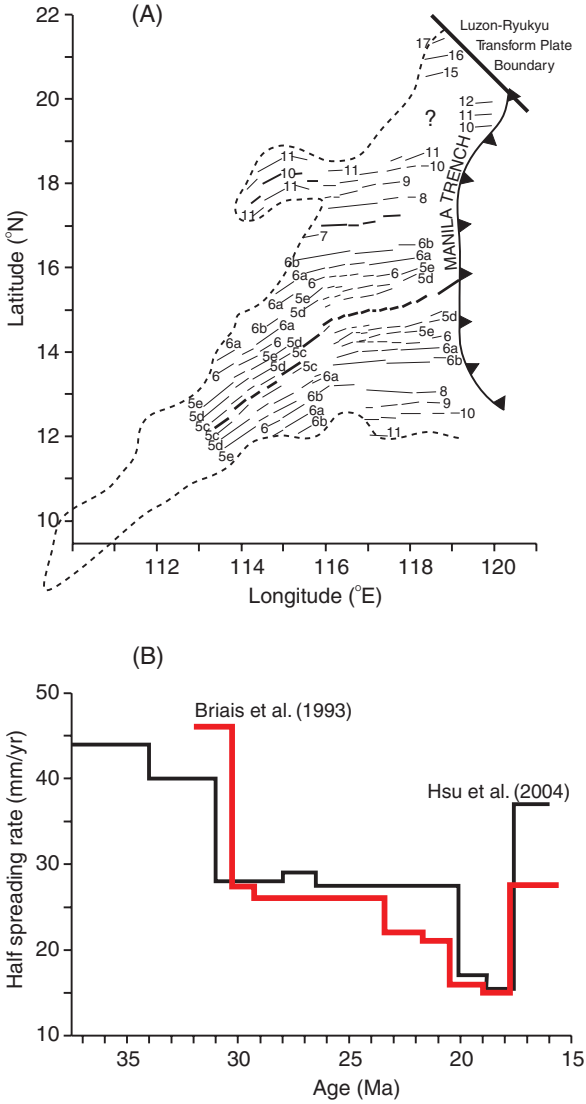

Fig. 2.25 (**A**) New interpretation of major magnetic anomaly lineaments in the central deep basin reveals an oceanic crust as old as 37 Ma at anomaly C17 in the NE corner of the deep basin. (**B**) Variations of half-spreading rates show a relative stable rate of ~28 mm/yr during the interval from 31 to 20 Ma. Both **A** and **B** are modified from Hsu et al. (2004)

A recent study of magnetic lineaments discovers that seafloor spreading in the northeastern corner of the SCS occurred much earlier at ∼37 Ma, during anomaly C17 (Hsu et al. 2004) (Fig. 2.25). The newly identified continent-ocean boundary (COB) is marked by the presence of a relatively low magnetization zone at the base of the continental slope, corresponding to the thinned portion of the continental crust. Hsu et al. (2004) suggested that the northern extension of the SCS oceanic crust is terminated by an inactive NW-SE trending trench-trench, left-lateral transform fault, called the Luzon-Ryukyu Transform Plate Boundary (LRTPB) (Fig. 2.25). The LRTPB was connected to the former southeast- dipping Manila Trench in the south and the northwest-dipping Ryukyu Trench in the north, and probably became inactive at ca. 20 Ma. These results indicate a half-spreading rate of 40–44 mm/yr from 37 to 31 Ma before stabilizing at ∼28 mm/yr in the early spreading history of the SCS (Fig. 2.25).

In the south, rifting lasted from Eocene (∼46 Ma) to early Miocene (∼21 − 19 Ma). The subsequent seafloor spreading caused a break-up hiatus of 3–5 myr, or the Mid-Miocene Unconformity widely recorded in many southern areas (ASCOPE 1981; Hutchison 2004) (Fig. 2.26). However, Mesozoic thrust anticlines recently found in the hinterland of the Nansha Block (Yan and Liu 2004) seem to support the existence of a NW-SE subduction zone already in the Mesozoic, as proposed originally by Holloway (1982). This subduction zone may further support the hypothesis that at least part of the present SCS, like many marginal seas in the western Pacific, was once a back-arc basin (Honza and Fujioka 2004). Nevertheless, the southeasterly extrusion of the Indochina subcontinent along the Red River Fault since the late Paleogene and the subsequent collision and subduction along the eastern SCS margin may have overridden some pre-existing geotectonic features (Hall 2002;

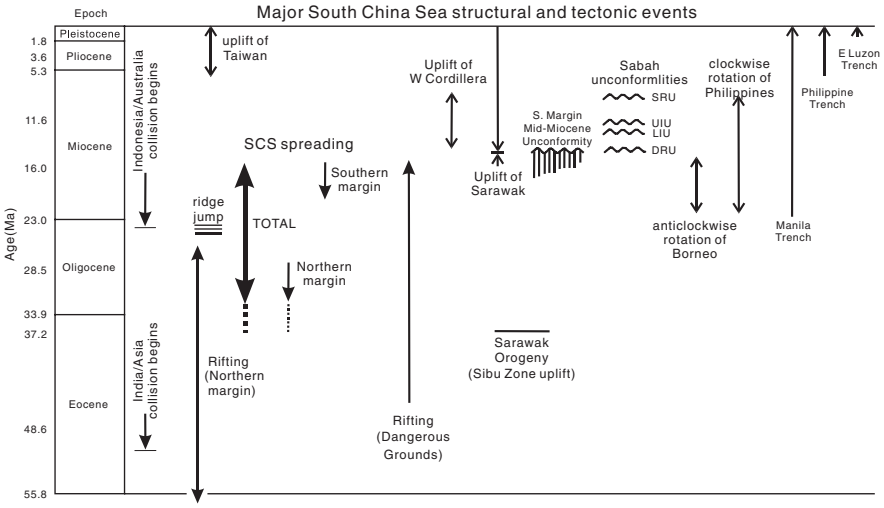

Fig. 2.26 Major structural and tectonic events in the SCS region since the Eocene are compiled mainly from Hall (2002), Hutchison (2004), and Yumul et al. (2003). Earliest seafloor spreading is now dated at ∼37 Ma, magnetic anomaly C17 (refer to Fig. 2.25)

Morley 2002) (Fig. 2.23). The southward extension of the Red River Fault to central Salawak along the Baram Line (Morley 2002) (Fig. 2.21) subdivided the relatively stable southwestern margin from the subduction zone in the southeastern and eastern SCS since the middle Miocene (Hutchison 2004; Hall and Morley 2004). Therefore, while post-rift sediment fill characterized the northern and southwestern margin, collision and subduction were the main features along the eastern margin especially in the last 5 myr (Fig. 2.26).

Therefore, available data indicate a stepwise opening of the SCS: ~37 Ma in the northeast, ~33—~31 Ma in the north and ~21 Ma or younger in central and southern parts (Fig. 2.26). The main driving force of seafloor spreading in the SCS may include the SE extrusion of the Indochina subcontinent due to Tibet uplift and slab pull from subduction of the eastern Asian margin including the Proto-SCS into the Philippine Sea Plate (Fig. 2.23).

Step-Wise Closure of the Sea Basin

However, the present shape and semi-enclosed nature of the SCS has not resulted from seafloor spreading, but from the post-spreading tectonic development. In the south, Australia-Asia collision began in Sulawesi at about 25 Ma, leading to the anti-clockwise rotation of Borneo and closure of the SCS in the south (Hall and Morley 2004) (Fig. 2.23). The rotation of the Philippine Sea Plate and the collision of the Luzon Arc with the Asian margin of the Eurasian Plate gave rise to the uplift of Taiwan, closing the SCS basin on the eastern side (Figs. 2.23 and 2.25). Sibuet et al. (2002, 2004) argued that the rise of Taiwan and the closure of the SCS in general may not require a rotating Philippine Sea Plate but a stronger push from the joint force of the Pacific and Australian plates. Subduction along the eastern margin leading to oblique arc-continent collision in northern Taiwan began at about 6.5 Ma, in the late Miocene (Huang et al. 1997).

The closure of the SCS basin is closely related to a change of the tectonic regime in SE Asia region, which also contributed to the closure of the water way between the Pacific and Indian oceans, the Indonesian seaway. Five barriers may have acted more significantly than others in blocking the Indonesian seaway as well as the closure of the SCS: (1) Banda Arc colliding with New Guinea at 11–9 Ma, (2) south Banda colliding with NW Australian margin at ~6 Ma, (3) Sula and (4) Seram blocks both migrating and repositioning during 5–3 Ma, and (5) the closing of the Molucca Sea at ~3 Ma (Linthout et al. 1997; Hall 2002; Zhou et al. 2004). A significant shoaling at ~10 Ma around Sulawesi was caused by collision of the continental fragments of Buton (part of the Indo-Australian Plate) and the Sundaland (Eurasian Plate). In Sulawesi, contemporary geochemical signatures shifted from indicating arc-volcanics to a subduction-modified mantle with a significant contribution from the subcontinental lithospheric mantle (Elburg and Foden 1999).

The emergence of Taiwan and the present Bashi Strait resulted from Luzon Arc/Eurasian Plate collision beginning ~6.5 Ma ago (Huang et al. 1997) (Fig. 2.26). A series of events were involving in the westward migration of collision (Sibuet

et al. 2004). In a review of collision, subduction and accretion events in the Philippines, Yumul et al. (2003) noted that Luzon onramped the SCS crust in the course of rotation and effectively converted the shear zone and bounded them into a subduction zone. Rangin et al. (1985) found the SCS oceanic crust of Oligocene age jammed into the Mindoro collision zone. The Taiwan accretionary prism includes a collision prism in the west and a subduction wedge in the east, due to a change of tectonic modes from intra-oceanic subduction to arc-continent collision and arc accretion (Huang et al. 1997). By ∼5 Ma, the northeastern end of the SCS oceanic crust at the present position off southern Taiwan and probably also some area in the Bashi Strait and further south along the Manila Trench had been completely subducted (Fig. 2.26).

Accompanying the rise of Taiwan was a series of neotectonic activities relating to collision and subduction in the SCS region (e.g., Liu Y. 1994). Lüdmann and Wong (1999) identified two main collision phases in the northern region: 5–3 Ma and 3–0 Ma. Pliocene faults are mainly ENE-WSW to NE-SW trending and strike-slip in nature, while recent faults are generally oriented NE-SW subparallel to the syn-rift faults. Most likely, the underwater part of the Bashi Strait, now at ∼2, 400 m water depth, has been acting as a barrier blocking Pacific bottom waters flowing into the SCS since ∼5 Ma. Therefore, the isolated SCS bottom water became colder and more corrosive, subsequently causing more severe carbonate dissolution at deep water localities (Chapter 6). Continued subduction along the east margin over the last 5 myr has turned the once open SCS to a semi-enclosed basin with the Bashi Strait as the only deep passage remaining to connect the sea basin with the West Pacific.

Arc-continent collision in the region since the middle Miocene has contributed to frequent volcanic activities along the eastern margin, although volcanism at the time of rifting was also common in the western Pacific arc region (Taylor and Natland 1995). Among a string of volcanoes in a long, mountainous Bicol Peninsula in southern Philippines, the peak of Mayon Volcano rises to a height of 2,525 m. Volcanoes in the north and west are relative rare and mostly confined to the Pliocene and Quaternary. As revealed by ODP Leg 184 drilling, volcanic ash layers appear to concentrate in three periods: ∼10 Ma, ∼6 Ma, and since ∼2 Ma (Wang P. et al. 2000). These periods also saw significant collision and uplift of island arcs and/or expansion of foreland basins along the east. For example, an unconformity of up to 10 myr in the Western Taiwan Foreland Basin separates the Quaternary sediments from the underlying eroded Miocene strata, indicating the development of a flexural forbulge associated with the transformation of tectonic settings from shelf-slope to foreland (Yu and Chou 2001).

Formation of Shelf-Slope Sedimentary Basins

About 40 Cenozoic sedimentary basins or basin-groups have been recognized in the SCS (Fig. 2.27). Some large basins are listed in Table 2.4 to reflect nomenclature complexity due to unsettled jurisdiction.

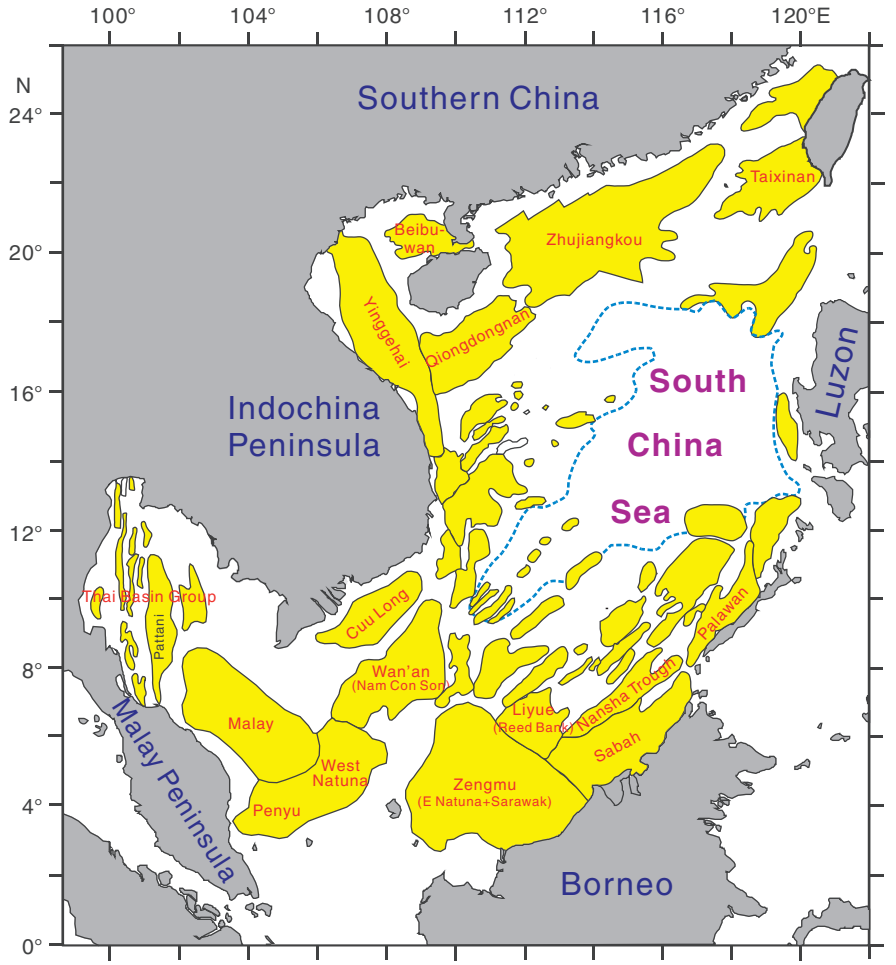

Fig. 2.27 Map shows distribution of Cenozoic sedimentary basins in the SCS as compiled from various sources. Refer to Table 2.4 for basin names and their synonyms

The development of shelf-slope basins closely accompanied Cretaceous-Paleogene rifting and subsequent seafloor spreading of the SCS (Fig. 2.26). A series of normal faults developed mostly in parallel to the shelf break, leading to the formation of most basins in the northern and southern SCS (Table 2.4). Faults in the west and northwest are often sheared or even strike-slip mainly in responding to the impact of the Red River Fault, and they control the general shape and development of the Yinggehai Basin and basins along the coast of Indochina Peninsula. Both sheared-faulted, the Yinggehai Basin in the northwest and Zengmu Basin in the south have a thickest sediment cover of over 14 km. Compressional or fore-arc basins are limited to the eastern margin, including the Sabah and Palawan basins (Jin 1989; Gong and Li 1997; Balaguru and Nichols 2004) (Table 2.4). Neotectonic activities along the northern margin include the development of ENE-WSW to

Table 2.4 Characteristics of major SCS basins are compiled from various sources

Center (°E/°N)	Basin	Area (km^2)	Formation character	Basement	[1] Syn-rift sediment	Post-rift sediment	Other phases
Northern South China Sea basins:							
119/22	Taixinan (SW Taiwan)	66,000	normal to foreland	Mz clastics	Paleogene	Oligo-Mio	Latest Mio (foreland)
114/20	Zhujiangkou (Pearl R Mouth)	147,000	normal faulting	Mesozoic granite	L Cret-E Oligo	L Oligo-Recent	
109/20	Beibuwan (Beibu Gulf)	38,000	normal faulting	Pz-Mz granite and clastics	Paleogene	Neogene	
108/18	Yinggehai (Song Hong)	113,000	transverse to sheared	Mz granite and clastics	Paleogene	Neogene	
110/17	Qiongdongnan (SE Hainan)	45,000	normal faulting	Mz granite and clastics	Paleogene	Neogene	
Southern South China Sea basins:							
107/10	Cuu Long	25,000	normal faulting	Late Mz granite	Eocene-Oligocene	L Oligo-Recent	
109/09	Wan'an (Nam Con Son)	90,000	normal to sheared	Mz granite, volc & clastics	Eocene-Miocene	Pliocene-Recent	
110/05	Zengmu (E Nat una + Sarawak)	170,000	foreland to compressed	Cret-Eocene turbidite			Oligo-Rec (foreland)
117/11	Liyue (Reed Bank)	20,000	foreland to compressed	Cretaceous-Eo turbidite			Oligo-Rec (foreland)
107/05	West Natuna	70,000	normal to inversional	Pre-Cenozoic meta volcanics	L Eo-E Oligo	L Oligo-Recent	L Oligo-Mio (inversion)
104/04	Penyu	10,000	normal faulting	Mesozoic volcanics	Oligocene	Miocene to Rec	M - L Mio (inversion)
103/07	Malay	80,000	normal to transverse	Pz-Mz igneous, meta clastics	Late Eo-E Oligo	L Oligo-E Mio	M - L Mio (inversion)
101/11	Thai Basin Gp (incl. Pattani)	75,000	normal to transverse	Pz-Mz igneous, clastics	Late Eo-E Mio	M Mio-Rec	
115/05	Sabah-Borneo	50,000	compressed to foreland	Mz-Pg marine sediment	Oligocene		M Mio-Rec (foreland)
118/10	Palawan	40,000	compressed to foreland	Mz-Pg marine sediment	Oligocene		M Mio-Rec (foreland)
115/07	Nansha Trough (NW Borneo T)	25,000	compressed to foreland	Mz-Pg marine sediment	Oligocene		M Mio-Rec (foreland)

[1] Pz = Paleozoic; Mz = Mesozoic; Pg = Paleogene; volc = volcanics; meta = metamorphosed.

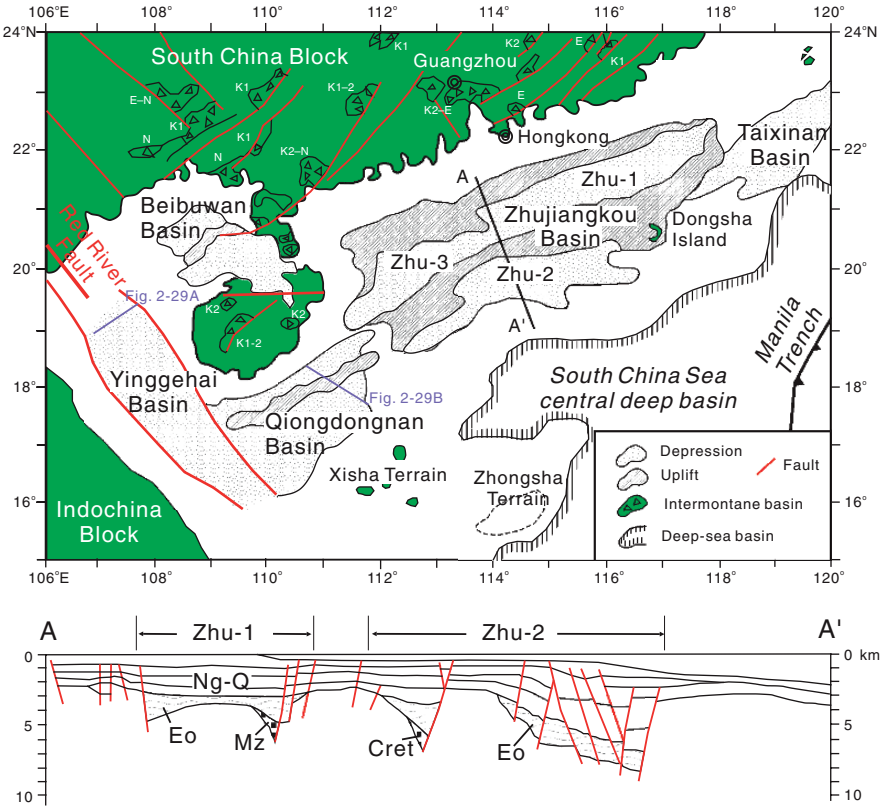

Fig. 2.28 Sketch map (*upper panel*) shows sedimentary basins in the northern margin. A cross section along line A-A′ (*lower panel*) illustrates the general characteristics of structural units and sediment packages in Zhu-1 and Zhu-2 depressions of the Zhujiangkou Basin (Ru et al. 1994)

NE-SW faults in the Pliocene and NE-SW faults in the Quaternary (Lüdmann and Wong 1999).

Major characteristics of several northern basins are illustrated in Figs. 2.28 and 2.29. Clearly, various stages of basin formation can be recognized for a specific basin, from rifting to thermal subsidence or even subsequent inversion (Pigott and Ru 1994; Madon and Watts 1998; Xie et al. 2006). Some stages are likely related also to preferential mantle lithospheric extension under the South China margin (Clift et al. 2001).

Although basins in a structural zone show similarities in both age and phases of formation, their subsidence rate and amplitude are often different (Fig. 2.30). Total subsidence over 14 km in the Yinggehai and Zengmu basins is highest, about half of which was attributed to structural subsidence. In other basins, total subsidence varies mostly between 3 and 8 km. Total subsidence < 5 km exists not only in more

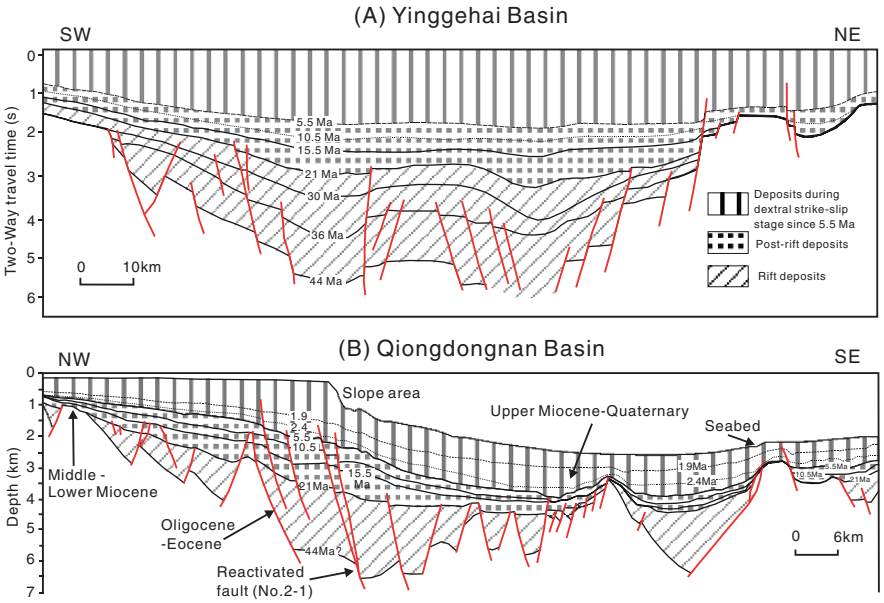

Fig. 2.29 Interpreted seismic sections for (**A**) the Yinggehai Basin and (**B**) the Qiongdongnan Basin show major structural features and reactivated faults along the slope break area (Xie et al. 2006). Refer to Fig. 2.28 for line locations

offshore basins in the north (such as those neighboring the Taixinan Basin) but also in the south including some sub-basins of the Malay Basin and Thai Basin Group (Fig. 2.30). Xie et al. (2006) recently found anomalous subsidence of 300–1,200 m in several northern basins probably induced by a late thermal cooling and renewed faulting since the late Miocene. However, late Miocene basin inversion was a main feature in the Malay Basin (Madon and Watts 1998) and other basins in the south and southeast, as well as in the Taixinan Basin (Lee et al. 1993). Inversion also caused dolomitization in the Malay Basin (Fig. 2.30).

Increases in subsidence rates concurred with major steps in the evolution of the SCS, especially at ~25 Ma and ~5 Ma. The 25 Ma event was related to the spreading ridge jump to southwest (Fig. 2.26), leading to a large scale regional subsidence and marine transgression along the northern margin (Gong and Li 1997). The 5 Ma event was largely responding to intensive collision and subduction along the eastern margin that also contributed to the rise of Taiwan. Smaller-scaled increases in subsidence rates appear to represent variations in individual basins due to local factors (Madon and Watts 1998; Wheeler and White 2002) (Fig. 2.30; see also Chapter 3). Increased subsidence often leads to increase in sedimentation rates if erosion in source areas was also strong (Clift et al. 2004).

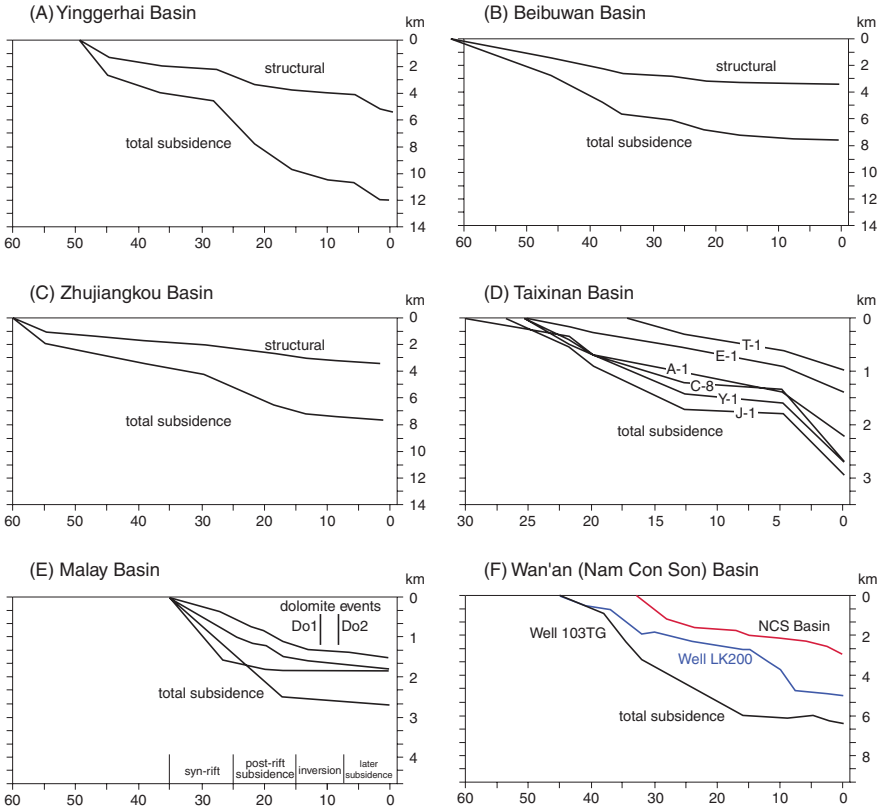

Fig. 2.30 Various subsidence trends are observed in SCS basins: (**A**) Yinggehai Basin (Gong and Li 1997), (**B**) Beibuwan Basin (Gong and Li 1997), (**C**) Zhujiangkou Basin (Gong and Li 1997), (**D**) Taixinan Basin (Lee et al. 1993), (**E**) Malay Basin (Madon and Watts 1998; dolomite events after Ali 1995), (**F**) Wan'an Basin and offshore Vietnam (based on Wheeler and White 2002; Nielsen et al. 1999)

Sediments of the SCS Shelf-Slope Basins: An Overview

The basins of the northern SCS shelf and slope often show a two-layer structure: the lower section characterized by syn-rift half-grabens filled with non-marine Paleogene sequences, and the upper section by a wide range of terrigenous and marine sediments deposited during Neogene subsidence (Figs. 2.28, 2.29, and 2.31). In the south and southwest, similar sedimentary structure can also be observed although the boundary between the rift and post-rift sediments mostly lies in the middle Miocene due to a delay in seafloor spreading there. As a prelude to Chapter 3 and Chapter 4, several important points on the major sedimentation characteristics of shelf to slope basins in the SCS can be generalized:

(1) The development of the marginal basins was associated with rifting and spreading, but the basal ages of basin sediments indicate that many basins were

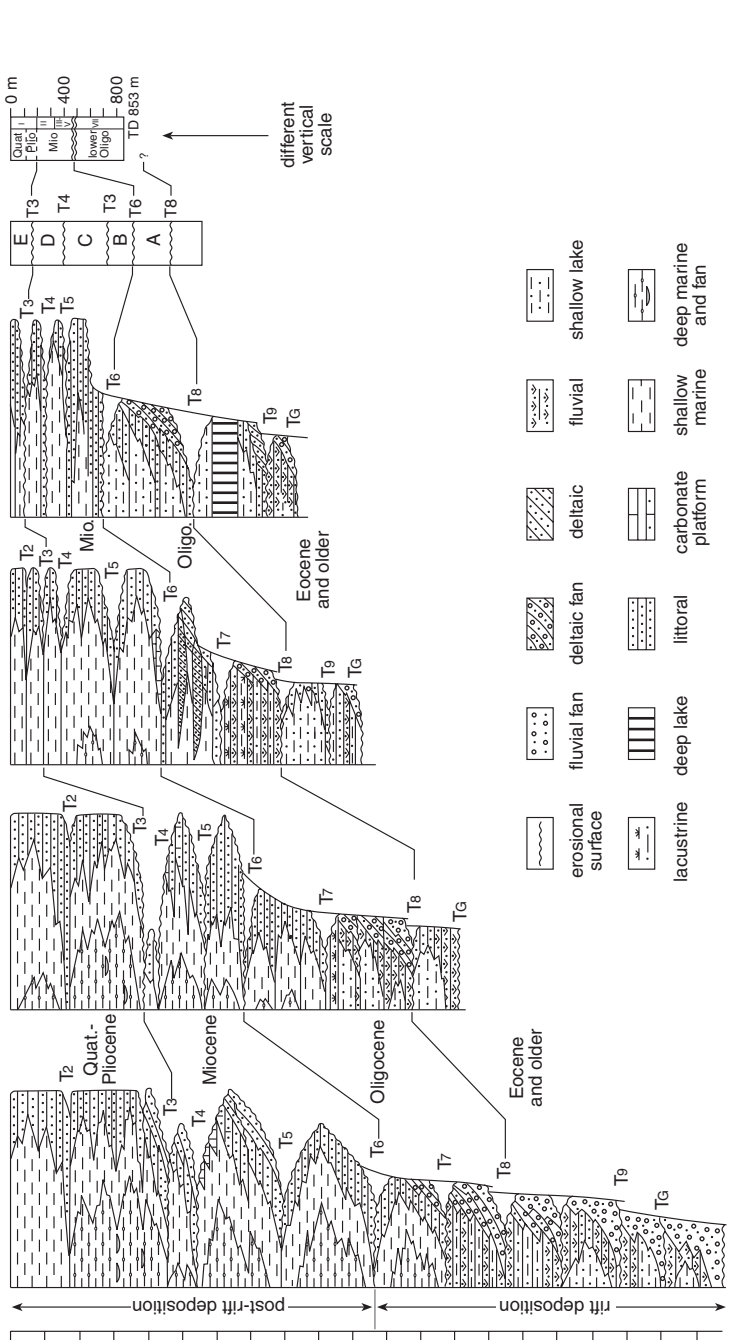

Fig. 2.31 Generalized lithostratigraphic columns show variations of lithofacies and sediment thickness in northern SCS basins (modified from Gong and Li 1997). T1 to TG are seismic reflectors representing unconformities. Taixinan Basin supersequences are after Lee et al. (1993). ODP Site 1148 sediment ages and lithostratigraphic units I to VII are after Wang P. et al. (2000) and shown with a different vertical scale

initiated before spreading and that the ages of individual basins vary (Table 2.4). For example, sedimentation began in the Paleocene-lower Eocene in the northwest and northeast, during the lower Oligocene in the north and in the south (Sunda shelf), and during the Paleocene in the southeastern Reeds Bank basin. Sediment accumulation was determined by basin locations relative to major sediment sources. The Zhujiangkou Basin received sediments mainly from the Pearl, while the Yinggehai Basin/Song Hong Basin and basins in the southwest were mainly fed by clastic sediments from the Red and Mekong rivers, respectively. Weathering of mountain ranges along the eastern-southeastern arc system also contributed a significant amount of sediment material to the nearby basins, especially during the Neogene (Clift et al. 2004) (Chapter 4).

(2) Non-marine fluvial and lacustrine sedimentation dominates the shelf basins in pre- and syn-rifting periods. Transition to marine sedimentation varies from late Oligocene-earliest Miocene in the north (Fig. 2.31) to middle Miocene in southern basins (Chapter 3). While global sea level has been generally declining throughout the late Eocene-Holocene period (Haq et al. 1987), these data indicate asynchronous shelf subsidence during the later phase of rifting in various parts of the SCS.

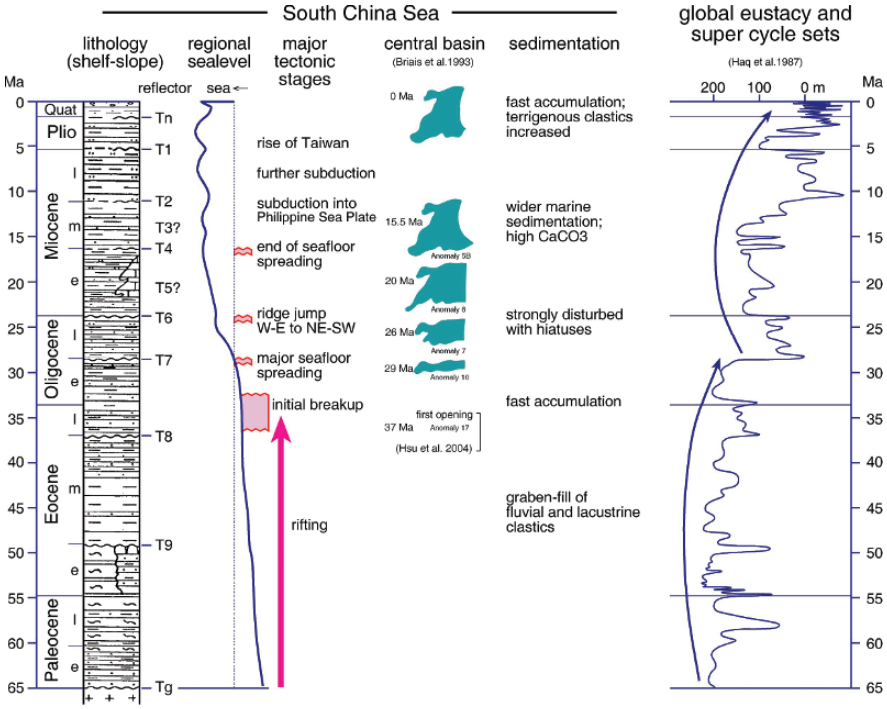

Fig. 2.32 Major features of sedimentary and tectonic events and deep basin formation in the SCS (synthesized from various sources) are compared with global eustatic curves (of Haq et al. 1987), showing tectonic imprints on regional sea level change

(3) Buried faults within basin sediments indicate that shelf-basin tectonics declined toward the end of rifting (Figs. 2.28 and 2.29). Meanwhile, marine inundation toward the end of rifting marked by widespread development of carbonate banks on the S-SE shelf (Chapter 3) was often accompanied by widespread unconformities (Fig. 2.26). Marine sedimentation interrupted by unconformities/seismic reflectors (Fig. 2.31) apparently reflect global sea level variations superimposed on differential local subsidence (Fig. 2.32).

Summary of Tectonics and Basin Formation

The semi-enclosed South China Sea evolved from late Cretaceous to Paleogene rifting, late Eocene to middle Miocene seafloor spreading, and post-spreading subduction and closing since the late Miocene. The opening of the SCS was mainly influenced by the extrusion of Indochina subcontinent due to Tibet uplift and slab pull due to subduction of the Asian continental crust into the Philippine Sea Plate. A Proto-SCS existed before rifting and spreading mainly along the present southeastern margin although its size and connection with other paleo-oceans are not clear. Based on magnetic anomaly lineament data from the northeast, the SCS first opened at ~37 Ma (anomaly C17), in the late Eocene (Fig. 2.25). A spreading ridge jump from nearly W-E to SW at 25–23 Ma caused widespread subsidence especially in the north. The central deep basin lying on an oceanic crust of ~8 km appears to have subsided to a maximum depth during the late Miocene-Pliocene (Chapter 6) when collision and subsidence along the eastern margin intensified.

Rifting in the south delayed until the Eocene-Miocene, and a breakup unconformity of 3–5 myr often underlies strata of 16 Ma and older ages. Since the middle Miocene, the southern margin west of the Baram line, a proposed extension of the Red River Fault, was tectonically more stable while the eastern margin has been subducting, subsequently causing the closure of the sea basin and rise of Taiwan in the last 5 myr.

Rifting opened sedimentary basins of various depths and sizes that are often characterized by distinctive syn-rift and post-rift sediment packages. Three kinds of basins can be identified: those normal faulted often parallel to the coast, those sheared often controlled by major lateral-strike or transverse fault zones, and those compressional often relating to subduction. The Yinggehai and Zengmu basins are deepest, with sediment fill of over 14 km, about half of which was induced by structural subsidence. Basin inversion is common in tectonically active regions since the late Miocene. In the north, faulting direction changed from NE-SW in the Miocene to ENE-WSW or NE-SW in the Pliocene to NE-SW in the Quaternary. Terrigenous clastic sediments are predominant in shelf-slope basins, while hemipelagic components increase down-slope to over 50% in the central deep basin.

Acknowledgments This work was supported by the Ministry of Science and Technology of China (NKBRSF Grant 2007CB815900) and the National Natural Science Foundation of China (Grants 40576031, 40621063 and 40631007).

References

ASCOPE (Asean Council on Petroleum) 1981. Tertiary Sedimentary Basins of the Gulf of Thailand and South China Sea: Stratigraphy, Structure and Hydrocarbon Occurrences. ASCOPE, Jakarta, Indonesia, 72pp.

Ali M.Y. 1995. Carbonate cement stratigraphy and timing of diagenesis in a Miocene mixed carbonate-clastic sequence, offshore Sabah, Malaysia: constraints from cathodoluminescence, geochemistry and isotope studies. Sedimentary Geol. 22: 191–214.

Balaguru A. and Nichols G. 2004. Tertiary stratigraphy and basin evolution, southern Sabah (Malaysian Borneo). J. Asian Earth Sci. 23: 537–554.

Barckhausen U. and Roeser H.A. 2004. Seafloor spreading anomalies in the South China Sea revisited. In: Clift P., Wang P., Kuhnt W. and Hayes D. (eds.), Continent-Ocean Interactions within East Asian Marginal Seas. AGU Geophys. Monogr. 149: 121–125.

Briais A., Patriat P. and Tapponnier P. 1993. Update interpretation of magnetic anomalies and seafloor spreading stages in the South China Sea: Implications for the Tertiary tectonics of southeast Asia. J. Geophys. Res. 98(B4): 6299–6328.

Chao S.Y., Shaw P.T. and Wu S.Y. 1996. El Nino modulation of the South China Sea circulation. Progr. Oceanogr. 38: 51–93.

Chen L. 1992. Features of the East Asian monsoon. In: Murakami M. and Ding Y. (eds.), Studies of Asian Monsoon in Japan and China. Meteorol. Res. Inst., Ibaraki, Japan, pp. 220–235.

Chen C.T.A., Wang S.L., Wang B.J. and Pai S.C. 2001. Nutrient budgets for the South China Sea basin. Mar. Chem. 75: 281–300.

Chen C.T.A. and Huang M.H. 1996. A mid-depth front separating the South China Sea water and the Philippine Sea water. J. Oceanogr. 52: 17–52.

Chu P.C. and Wang G. 2003. Seasonal variability of thermohaline front in the central South China Sea. J. Oceanogr. 59: 65–78.

Clift P.D. and Lin J. 2001. Preferential mantle lithospheric extension under the South China margin. Mar. Petroleum Geol. 18: 929–945.

Clift P.D., Shimizu N., Layne G.D. and Blusztajn J. 2001. Tracing patterns of unroofing in the Early Himalaya through microprobe Pb isotope analysis of detrital K-feldspars in Indus Molasse, India. Earth Planet. Sci. Lett. 188: 475–491.

Copeland P. 1997. The when and where of the growth of the Himalaya and the Tibetan Plateau. In: Ruddiman W.F. (ed.), Tectonic Uplift and Climate Change. Plenum, New York, pp. 19–40.

Clift P.D., Layne G.D. and Blusztajn J. 2004. Marine sedimentary evidence for monsoon strengthening, Tibetan uplift and drainage evolution in East Asia. In: Clift P., Wang P., Kuhnt W. and Hayes D. (eds.), Continent-Ocean Interactions within East Asian Marginal Seas. AGU Geophys. Monogr. 149: 255–282.

Ding Y., Li C. and Liu Y. 2004. Overview of the South China Sea Monsoon Experiment. Adv. Atmospheric Sci. 21: 343–360.

Dong L., Su J., Wong L.A., Cao Z. and Chen J.C. 2004. Seasonal variations and dynamics of the Pearl River plume. Continental Shelf Res. 24: 1761–1777.

Du Bois E.P. 1985. Review of principal hydrocarbon-bearing basins around the South China Sea. Bull. Geol. Soc. Malaysia 18: 167–209.

Elburg M.A. and Foden J. 1999. Geochemical response to varying tectonic settings: An example from southern Sulawesi (Indonesia). Geochim. Cosmochim. Acta 63: 1155–1172.

Fan W. and Menzies M.A. 1992. The lithospheric mantle composition of volcanism in extension settings: the geochemical evidence of Cenozoic basalts in Leiqiong area. In: Liu R. (ed.), The Ages and Geochemistry of Cenozoic Volcanic Rocks in China. Seismological Press, Beijing, pp. 320–329.

Fang G.H., Fang W.D., Fang Y. and Wang K. 1998. A survey of studies on the South China Sea upper ocean circulation. Acta Oceanogr. Taiwanica 37: 1–16.

Fang W., Fang G., Shi P., Huang Q. and Xie Q. 2002. Seasonal structures of upper layer circulation in the southern South China Sea from in situ observations. J. Geophys. Res. 107: C11 3202, doi:10.1029/2002 JC001343.

Gilley L.D., Harrison T.M., Leloup P.H., Ryerson F.J., Lovera O.M. and Wang J.H. 2003. Direct dating of left-lateral deformation along the Red River shear zone, China and Vietnam. J. Geophys. Res. 108(B2): 2127, doi:10.1029/2001JB001726.

Gong G.C., Liu K.K., Liu C.T. and Pai S.C. 1992. The chemical hydrography of the South China Sea west of Luzon and a comparison with the West Philippine Sea. Terr. Atmos. Ocean. Sci. (TAO) Taipei 13: 587–602.

Gong Z. and Li S. (eds.). 1997. Continental Margin Basin Analysis and Hydrocarbon Accumulation of the Northern South China Sea. China Sci. Press, Beijing, 510pp (in Chinese).

Gradstein F., Ogg J. and Smith A. (eds.). 2004. A Geologic Time Scale 2004. Cambridge Univ. Press, Cambridge, 589pp.

Hall R. 2002. Cenozoic geological and plate tectonic evolution of SE Asia and the SW Pacific: computer-based reconstructions, model and animations. J. Asian Earth Sci. 20: 353–431.

Hall R. and Morley C.K. 2004. Sundaland basins. In: Clift P., Wang P., Kuhnt W. and Hayes D. (eds.), Continent-Ocean Interactions within East Asian Marginal Seas. AGU Geophys. Monogr. 149: 55–85.

Harrison T.M., Copeland P., Kidd W.S.F. and Yin A. 1992. Raising Tibet. Science 255: 1663–1670.

Haq B.U., Hardenbol J. and Vail P.R. 1987. Chronology of fluctuating sea levels since the Triassic (250 million years ago to present). Science 235: 1156–1167.

Hawkins J.W., Lonsdale P.F., Macdougall J.D. and Volpe A.M. 1990. Petrology of the axial ridge of Mariana Trough backarc spreading center. Earth Planet. Sci. Lett. 100: 226–250.

Hayes D.S. and Nissen S.S. 2005. The South China Sea margins: Implications for rifting contrasts. Earth Planet. Sci. Lett. 237: 601–616.

Hayes D.E., Nissen S.S., Buhl P., Diebold J., Yao B., Zeng W. and Chen Y. 1995. Throughgoing crustal faults along the northern margin of the South China Sea and their role in crustal extension. J. Geophys. Res. 100: 22435–22446.

Holloway N.H. 1982. North Palawan Block, Philippines, its relation to Asian mainland and role in evolution of South China Sea. AAPG Bull. 66: 1355–1383.

Honza E. and Fujioka K. 2004. Formation of arcs and backarc basins inferred from the tectonic evolution of Southeast Asia since the Late Cretaceous. Tectonophysics 384: 23–53.

Hsu M.K., Liu A.K. and Liu C. 2000. A study of internal waves in the China Seas and Yellow Sea using SAR. Continental Shelf Res. 20: 389–410.

Hsu S.K., Yeh Y.C., Doo W.B. and Tsai C.H. 2004. New bathymetry and magnetic lineations identifications in the northernmost South China Sea and their tectonic implications. Mar. Geophys. Res. 25: 29–44.

Hsueh Y. and Zhong L. 2004. A pressure-driven South China Sea warm current. J. Geophys. Res. 109: C09014, doi:10.1029/2004JC002374.

Huang C.Y., Wu W.Y., Chang C.P., Tsao S., Yuan P.B., Lin C.W. and Xia K.Y. 1997. Tectonic evolution of accretionary prism in the arc-continent collision terrane of Taiwan. Tectonophysics 281: 31–51.

Hutchison C.S. 2004. Marginal basin evolution: the southern South China Sea. Mar. Petroleum Geol. 21: 1129–1148.

Jin Q. (ed.). 1989. The Geology and Petroleum Resources in the South China Sea. Geol. Publ. House, Beijing, 417pp (in Chinese).

Lallemand S., Heuret A. and Boutelier D. 2005. On the relationships between slab dip, back-arc stress, upper plate absolute motion, and crustal nature in subduction zones. Geochem. Geophys. Geosyst. 6: Q09006, doi:10.1029/2005GC000917.

Lee T.-Y. and Lawver L.A. 1994. Cenozoic plate reconstruction of the South China Sea region. Tectonophysics 235: 149–180.

Lee T.-Y., Tang C.-H., Ting J.-S. and Hsu Y.-Y. 1993. Sequence stratigraphy of the Tainan Basin, offshore southwestern Taiwan. Petroleum Geol. Taiwan 28: 119–158.

Leloup P.H., Arnaud N., Lacassin R., Kienast J.R., Harrison T.M., Phan Trong T.T., Replumaz A. and Tapponnier T. 2001. New constraints on the structure, thermochronology, and timing of the Ailao Shan-Red River shear zone, SE Asia. J. Geophys. Res. 106: 6683–6732.

Li C., Zhou Z., Hao H., Chen H., Wang J., Chen B. and Wu J. 2008. Late Mesozoic tectonic structure and evolution along the present-day northeastern South China Sea continental margin. J. Asian Earth Sci. 31: 546–561.

Linthout K., Helmers H. and Sopaheluwakan J. 1997. Late Miocene obduction and microplate migration around the southern Banda Sea and the closure of the Indonesian Seaway. Tectonophysics 281: 17–3.

Liu Z., Wang P., Wang C., Shao L. and Huang W. 2001. Paleotopography of China during the Cenozoic: a preliminary study. Geol. Rev. 47(5): 467–475 (in Chinese).

Liu A.K., Chang Y.S., Hsu M.-K. and Liang N.K. 1998. Evolution of nonlinear internal waves in the East and South China Seas. J. Geophys. Res. 103(C4): 7995–8008.

Liu Q., Yang H. and Wang Q. 2000. Dynamic characteristics of seasonal thermocline in the deep sea region of the South China Sea. Chinese J. Oceanol. Limnol. 18(2): 104–109.

Liu K.-K., Chao S.-Y., Shaw P.-T., Gong G.-C., Chen C.-C. and Tang T.Y. 2002. Monsoon-forced chlorophyll distribution and primary production in the South China Sea: observations and a numerical study. Deep-Sea Res. I 49: 1387–1412.

Liu Q., Jiang X., Xie S.-P. and Liu W.T. 2004. A gap in the Indo-Pacific warm pool over the South China Sea in boreal winter: Seasonal development and interannual variability. J. Geophys. Res. 109: C07012, doi: 10.1029/2003JC002179.

Liu C.-T., Pinkel R., Hsu M.-K., Klymak J.M., Chen H.-W. and Villanov C. 2006. Nonlinear internal waves from the Luzon Strait. EOS, Trans. AGU 87(42): 449–451.

Lüdmann T. and Wong H.K. 1999. Neotectonic regime on the passive continental margin of the northern South China Sea. Tectonophysics 311: 113–138.

Madon M.B. and Watts A.B. 1998. Gravity anomalies, subsidence history and the tectonic evolution of the Malay and Penyu Basins (offshore Peninsular Malaysia). Basin Res. 10: 375–392.

Metzger E.J. and Hurlburt H.E. 1996. Coupled dynamics of the South China Sea, the Sulu Sea, and the Pacific Ocean. J. Geophys. Res. 101: 12331–12352.

Metzger E.J. and Hurlburt H.E. 2001. The nondeterministic nature of Kuroshio penetration and eddy shedding in the South China Sea. J. Phys. Oceanogr. 31: 1712–1732.

Morley C.K. 2002. A tectonic model for the Tertiary evolution of strike-slip faults and rift basins in SE Asia. Tectonophysics 347: 189–215.

Nielsen L.H., Mathiesen A., Bidstrup T., Vejbñk O.V., Dien P.T. and Tiem P.V. 1999. Modeling of hydrocarbon generation in the Cenozoic Song Hong Basin, Vietnam: a highly prospective basin. J. Asian Earth Sci. 17: 269–294.

Nissen S.S., Hayes D.E., Buhl P., Diebold J., Bochu Y., Weijun Z. and Chen Y. 1995. Deep penetration seismic soundings across the northern margin of the South China Sea, J. Geophys. Res. 100(B11): 22407–22434.

Nitani, H. 1972. Beginning of the Kuroshio. In: Stommel H., Yoshida K.(eds.), Kuroshio: Its Physical Aspects. University of Washington Press, Seattle, pp. 129–163.

Pigott J.D. and Ru K. 1994. Basin superposition on the northern margin of the South China Sea. Tectonophysics 235: 27–50.

Pubellier M. and Chan L.S. (eds.). 2006. Morphotectonic Map of Cenozoic Structures of the South China-Northern Vietnam Coastal Region. Output-express Print Office. Hong Kong, 16pp (CD-ROM).

Pubellier M., Ego F., Chamot-Rooke N. and Rangin C. 2003. The building of pericratonic mountain ranges: structural and kinematic constraints applied to GIS-based reconstructions of SE Asia. Bull. Soc. Geol. France 174: 561–584.

Pubellier M., Monnier C., Maury R. and Tamayo R. 2004. Plate kinematics, origin and tectonic emplacement of supra-subduction ophiolites in SE Asia. Tectonophysics 92: 9–36.

Pubellier M., Rangin C., Ego F., et al. 2005. Altas of the Margin of SE Asia. Soc. Geol. France/AAPG Spec. Publ. 176 (CD-ROM).

Qiu X., Ye S., Wu S., Shi X., Zhou D., Xia K. and Flueh R. 2001. Crustal structure across the Xisha Trough, northwestern South China Sea. Tectonophysics 341: 179–193.

Qu T. 2000. Upper-layer circulation in the South China Sea. J. Phys. Oceanogr. 30: 1450–1460.

Qu T. 2002. Evidence for water exchange between the South China Sea and the Pacific Ocean through the Luzon Strait. Acta Oceanol. Sinica 21(2): 175–185.
Qu T., Girton J.B. and Whitehead J.A. 2006. Deepwater overflow through Luzon Strait. J. Geophys. Res. 111: C01002, doi: 10.1029/2005JC003139.
Qu T., Mitsudera H. and Yamagata T. 2000. Intrusion of the North Pacific waters into the South China Sea. J. Geophys. Res. 105(C3): 6415–6424.
Rangin C., Stephan J.F. and Mueller C. 1985. Middle Oligocene oceanic crust of South China Sea jammed into Mindoro collision zone (Philippines). Geology 13: 425–428.
Ru K. and Pigott J.D. 1986 Episodic rifting and subsidence in the South China Sea. AAPG Bull. 70: 1136–1155.
Ru K., Zhou D. and Chen H. 1994. Basin evolution and hydrocarbon potential of the northern South China Sea. In: Zhou D., Liang Y. and Zeng C. (eds.), Oceanology of China Seas. Kluwer Press, New York, vol. 2, pp. 361–372.
Schlüter H.U., Hinz K. and Block M. 1996. Tectono-stratigraphic terranes and detachment faulting of the South China Sea and Sulu Sea. Mar. Geol. 130: 39–78.
Shaw P.T. 1996. Winter upwelling off Luzon in the Northeastern South China Sea. J. Geophys. Res. 101: 16435–16448.
Shaw P.T. and Chao S.Y. 1994. Surface circulation in the South China Sea. Deep-Sea Res. I 41: 1663–1683.
Shi P., Du Y.,Wang D.X. and Gan Z.J. 2001. Annual cycle of mixed layer in South China Sea. Tropical Oceanol. 20: 10–17 (in Chinese).
Sibuet J.C., Hsu S.K. and Debayle E. 2004. Geodynamic context of the Taiwan orogen. In: Clift P., Wang P., Kuhnt W. and Hayes D. (eds.), Continent-Ocean Interactions within East Asian Marginal Seas. AGU Geophys. Monogr. 149: 127–158.
Sibuet J.C., Hsu S.K., Le Pichon X., Le Formal J.P. and Reed D. 2002. East Asia plate tectonics since 15 Ma: constraints from the Taiwan region. Tectonophysics 344: 103–134.
Su J. 2004. Overview of the South China Sea circulation and its influence on the coastal physical oceanography outside the Pearl River Estuary. Continental Shelf Res. 24: 1745–1760.
Tapponnier P., Peltzer G. and Armijo R. 1986. On the mechanics of the collision between India and Asia. In: Coward M.P. and Ries A.C. (eds.), Collision Tectonics. Blackwell, Oxford, pp. 115–157.
Tapponnier P., Peltzer G., Le Dain A.Y., Armijo R. and Cobbold P. 1982. Propagating extrusion tectonics in Asia: new insights from simple experiments with plasticine. Geology 10: 611–616.
Tapponnier P., Xu Z., Roger F., Meyer B., Arnaud N., Wittlinger G. and Yang J. 2001. Oblique stepwise rise and growth of the Tibet Plateau. Science 294: 1671–1677.
Taylor B. and Hayes D.E. 1980. The tectonic evolution of the South China Sea Basin. In: Hayes D.E. (ed.), The Tectonic and Geologic Evolution of Southeast Asian Seas and Islands. AGU Geophys. Monogr., Washington, D.C., pp. 89–104.
Taylor B. and Hayes D.E. 1983. Origin and history of the South China Sea basin. In: Hayes D.E. (ed.), The Tectonics and Geologic Evolution of Southeast Asian Seas and Islands: Part 2. AGU Geophys. Monogr., Washington, D.C., pp. 23–56.
Taylor B. and Natland J. (eds.). 1995. Active Margins and Marginal Basins of the Western Pacific. AGU Geophys. Monogr., Washington, D.C., 88, p. 417.
Tian J.W., Yang Q., Liang X., Xie L., Hu D., Wang F. and Qu T. 2006. Observation of Luzon Strait transport. Geophys. Res. Lett. 33: L19607, doi: 10.1029/2006GL026272.
Wang C. 1996. Sequence stratigraphic analysis of marine Miocene formations in the Pearl River Mouth Basin and its significance. China Offshore Oil Gas (Geol.) 10(5): 279–288 (in Chinese).
Wang P. 1999. Response of Western Pacific marginal seas to glacial cycles: Paleoceanographic and sedimentological features. Mar. Geol. 156: 5–39.
Wang L., Koblinsky C.J. and Howden S. 2000. Mesoscale variability in the South China Sea from the TOPEX/Poseidon altimetry data. Deep-Sea Res. I 47: 681–708.
Wang P., Prell W.L., Blum P. (eds.). 2000. Proc. ODP, Init. Repts, Vol. 184 [CD-ROM]. Ocean Drilling Program, Texas A&M University, College Station TX 77845–9547, USA.

Wang D., Du Y. and Shi P. (eds.). 2002. Climatological Atlas of Physical Oceanography in the Upper Layer of the South China Sea. Meteorol. Press, Beijing, 168pp (in Chinese).
Wang G., Su J. and Chu P.C. 2003. Mesoscale eddies in the South China Sea observed with altimeter data. Geophys. Res. Lett. 30(21): 2121, doi: 10.1029/2003GL018532.
Wang R., Clemens S., Huang B. and Chen M. 2003. Late Quaternary paleoceanographic changes in the northern South China Sea (ODP Site 1146): radiolarian evidence. J. Quat. Sci. 18(8): 745–756.
Wang B., Clemens S.C. and Liu P. 2003. Contrasting the Indian and East Asian monsoons: implications on geological timescales. Mar. Geol. 201: 5–21.
Wang P. 2004. Cenozoic deformation and the history of sea-land interactions in Asia. In: Clift P., Wang P., Kuhnt W. and Hayes D. (eds.), Continent-Ocean Interactions in the East Asian Marginal Seas. AGU Geophys. Monogr. 149: 1–22.
Wang G., Chen D. and Su J. 2006. Generation and life cycle of the dipole in the South China Sea summer circulation. J. Geophys. Res. 111: C06002, doi: 10.1029/2005JC003314.
Wheeler P. and White N. 2002. Measuring dynamic topography: An analysis of Southeast Asia. Tectonics 21: 1040, doi:10.1029/2001TC900023.
Wong G.T.F., Ku T.L., Mulholland M., Tseng C.M. and Wang D.P. 2007a. The South East Asian Time-series Study (SEATS) and the biogeochemistry of the South China Sea-An overview. Deep-Sea Res. II 54: 1434–1447.
Wong G.T.F., Tseng C.M., Wen L.S. and Chung S.W. 2007b. Nutrient dynamics and nitrate anomaly at the SEATS station. Deep-Sea Res. II 54: 1528–1545.
Wyrtki K. 1961. Physical oceanography of the Southeast Asian waters. NAGA, La Jolla, Calif., Rept. 2: 1–195.
Xia K.Y. and Zhou D. 1993. The geophysical characteristics and evolution of northern and southern margins of the South China Sea. Geol. Soc. Malaysia Bull. 33: 223–240.
Xia B., Zhang Y., Cui X.J., Liu B.M., Xie J.H., Zhang S.L. and Lin G. 2006. Understanding of the geological and geodynamic controls on the formation of the South China Sea: A numerical modelling approach. J. Geodynamics 42: 63–84.
Xie S.P., Xie Q., Wang D. and Liu W.T. 2003. Summer upwelling in the South China Sea and its role in regional climate variations. J. Geophys. Res. 108(C8): 3261, doi: 10.1029/2003JC00 1867.
Xie X., Müller R.D, Li S., Gong Z. and Steinberger B. 2006. Origin of anomalous subsidence along the Northern South China Sea margin and its relationship to dynamic topography. Mar. Petroleum Geol. 23: 745–765.
Yang H.J. and Liu Q.Y. 1998. The seasonal features of temperature distributions in the upper layer of the South China Sea. Oceanol. Limn. Sinica 29: 501–507 (in Chinese).
Yan P. and Liu H. 2004. Tectonic-stratigraphic division and blind fold structures in Nansha waters, South China Sea. J. Asian Earth Sci. 24: 337–348.
Yan P., Zhou D. and Liu Z. 2001. A crustal structure profile across the northern continental margin of the South China Sea. Tectonophysics 338: 1–21.
Yao B. 1996. Tectonic evolution of the South China Sea in the Cenozoic. Mar. Geol. Quat. Geol. 16(2): 1–13 (in Chinese).
Yao B., Wan L. and Wu N. 2005. Cenozoic tectonic evolution and the 3D structure of the lithosphere of the South China Sea. Geol. Bull. China 24: 1–8 (in Chinese).
Yeh Y.C. and Hsu S.K. 2004. Crustal structures of the northernmost South China Sea: Seismic reflection and gravity modeling. Mar. Geophys. Res. 25: 45–61.
Yuan D.L. 2002. A numerical study of the South China Sea deep circulation and its relation to the Luzon Strait transport. Acta Oceanol. Sinica 21: 187–202.
Yumul G.P. Jr., Dimalanta C.B., Tamayo R.A. Jr. and Maury R.C. 2003. Collision, subduction and accretion events in the Philippines: A synthesis. Island Arc 12: 77–91.
Yu H.S. and Chou Y.W. 2001. Characteristics and development of the flexural forebulge and basal unconformity of Western Taiwan Foreland Basin. Tectonophysics 333: 277–291.

Zhou D., Ru K. and Chen H.Z. 1995. Kinematics of Cenozoic extension on the South China Sea continental margin and its implications for the tectonic evolution of the region. Tectonophysics 251: 161–177.

Zhou Z., Jin X., Wang L., Jian Z. and Xu C. 2004. Two closures of the Indonesian seaway and its relationship to the formation and evolution of the western Pacific warm Pool. Mar. Geol. Quat. Geol. 24: 7–14 (in Chinese).

Zhu B. and Wang H. 1989. Nd-Sr-Pb isotope and chemical evidence for the volcanism with MORB-OIB source characteristics in the Leiqiong area, China. Geochimica 18: 193–201.